Supplementary Information for: COVID-19 virtual patient cohort reveals immune mechanisms driving disease outcomes

Adrianne L. Jenner, Rosemary A. Aogo, Sofia Alfonso, Vivienne Crowe, Amanda P. Smith, Penelope A. Morel, Courtney L. Davis, Amber M. Smith, Morgan Craig

Correspondence to: morgan.craig@umontreal.ca

In the Supplementary Information, we detail the full model equations (Section S1), the parameters and their values (Section S2), and how parameters were estimated (Section S3-S5). Parameters in the model were either obtained from the literature (Section S3), through fitting to dose response data (Section S4.1) or through fitting to time-series measurements (Section S4.2). Remaining parameters were estimated through calculating homeostasis (Section S5). Validation against human SARS-CoV-2 infection measurements, and further information for the sensitivity analysis and virtual cohort simulations is also provided (Section S6). A summary of all variables and parameters in the full model (**Eqs. S1-S22**) can be found in **Table S1**.

S1. Mathematical model of the immune response to SARS-CoV-2

To model the immune response to SARS-CoV-2 infection, we constructed a system of ordinary and delay differential equations (**Figure 1, Main Text**). The model considers a population of susceptible lung cells (S) that become infected (I) by SARS-CoV-2 virus (V). Infected cells become damaged or dead (D) through the virus induced lysis or immune involvement. Upon infection, cells begin secreting type I IFN (F_U, F_B)which reduces viral infection and results in cells resistant to virus infection (R).

Alveolar macrophages ($M_{\Phi R}$) are activated by infected or dead cells and become inflammatory macrophages ($M_{\Phi I}$) and begin secreting IL-6 (L_U, L_B) and GM-CSF (G_U, G_B). Monocytes (M) are recruited by the presence of infected cells and stimulated by GM-CSF to differentiate into inflammatory macrophages. Neutrophils (N) are recruited by G-CSF (C_U, C_B) and contribute to bystander death of epithelial cells through the release of reactive oxygen species (ROS). $CD8^+$ T cells (T) are recruited after a delay from initial infection and induce apoptosis in infected cells. Bound and unbound concentrations are modelled explicitly. Equations for these interactions are given below:

$$\frac{dV}{dt} = pI - \delta_{V,M\Phi} M_{\Phi I} V - \delta_{V,N} N V - d_V V, \tag{S1}$$

$$\frac{dS}{dt} = \lambda_S \left(1 - \frac{S + I + R + D}{S_{max}}\right) S - \beta S V - \frac{\rho \delta_N S N^{h_N}}{N^{h_N} + {IC_{50,N}}^{h_N}}, \tag{S2}$$

$$\frac{dI}{dt} = \frac{\beta \epsilon_{F,I}}{F_B + \epsilon_{F,I}} S(t - \tau_I) V(t - \tau_I) - d_I I - \frac{\delta_N I N^{h_N}}{N^{h_N} + {IC_{50,N}}^{h_N}} - \delta_{I,M\Phi} M_{\Phi I} I - \delta_{I,T} T I, \tag{S3}$$

$$\frac{dR}{dt} = \lambda_S \left(1 - \frac{S + I + R + D}{S_{max}}\right) R + \frac{\beta F_B}{F_B + \epsilon_{F,I}} S(t - \tau_I) V(t - \tau_I) - \frac{\rho \delta_N R N^{h_N}}{N^{h_N} + {IC_{50,N}}^{h_N}}, \tag{S4}$$

$$\frac{dD}{dt} = d_I I + \frac{\delta_N (\rho S + \rho R + I) N^{h_N}}{N^{h_N} + {IC_{50,N}}^{h_N}} + \delta_{I,M\Phi} (M_{\Phi I}) I + \delta_{I,T} T I - d_D D + \left(\delta_{M\Phi,\mathrm{D}} - \delta_{D,M\Phi}\right)(M_{\Phi R} + M_{\Phi I}) D, \tag{S5}$$

$$\frac{dM_{\Phi R}}{dt} = -a_{I,M\Phi} M_{\Phi R} (I + D) - \delta_{M\Phi,\mathrm{D}} D M_{\Phi R} + \left(1 - \frac{M_{\Phi R}}{M_{\Phi max}}\right) \frac{\lambda_{M_\Phi} M_{\Phi I}}{V + \epsilon_{V,M\Phi}} - d_{M\Phi_R} M_{\Phi R}, \tag{S6}$$

$$\frac{dM_{\Phi I}}{dt} = a_{I,M\Phi}M_{\Phi R}(I+D) + \frac{p_{M_{\Phi I},G}G_B^{\,h_{M,M\Phi}}M}{G_B^{\,h_{M,M\Phi}} + \epsilon_{G,M_{\Phi I}}^{\,h_{M,M\Phi}}} + \frac{p_{M_{\Phi I},L}L_B M}{L_B + \epsilon_{L,M_\Phi}} - d_{M_{\Phi I}}M_{\Phi I} - \delta_{M\Phi,\mathrm{D}}DM_{\Phi I} - \left(1 - \frac{M_{\Phi R}}{M_{\Phi max}}\right)\frac{\lambda_{M_\Phi}M_{\Phi I}}{V + \epsilon_{V,M\Phi}}, \quad S7$$

$$\frac{dM}{dt} = \left(M^*_{prod} + \left(\psi_M^{max} - M^*_{prod}\right)\frac{G_B^{\,h_M}}{G_B^{\,h_M} + \epsilon_{G,M}^{\,h_M}}\right)M_R + \frac{p_{M,I}IM}{I + \epsilon_{I,M}} - \frac{p_{M_{\Phi I},G}G_B^{\,h_{M,M\Phi}}M}{G_B^{\,h_{M,M\Phi}} + \epsilon_{G,M_{\Phi I}}^{\,h_{M,M\Phi}}} - \frac{p_{M_{\Phi I},L}L_B M}{L_B + \epsilon_{L,M_\Phi}} - d_M M, \quad S8$$

$$\frac{dN}{dt} = \left(N^*_{prod} + \left(\psi_N^{max} - N^*_{prod}\right)\frac{C_{BF} - C^*_{BF}}{C_{BF} - C^*_{BF} + \epsilon_{C,N}}\right)N_R + \frac{p_{N,L}L_B}{L_B + \epsilon_{L,N}} - d_N N, \quad S9$$

$$\frac{dT}{dt} = \frac{p_{T,I}I(t-\tau_T)\epsilon_{L,T}}{L_B + \epsilon_{L,T}} + \frac{p_{T,F}F_B T}{F_B + \epsilon_{F,T}} - d_T T, \quad S10$$

$$\frac{dL_U}{dt} = \frac{p_{L,I}I}{I + \eta_{L,I}} + \frac{p_{L,M_{\Phi I}}M_{\Phi I}}{M_{\Phi I} + \eta_{L,M_{\Phi I}}} + \frac{p_{L,M}M}{M + \eta_{L,M}} - k_{lin_L}L_U - k_{B_L}\left((M+N+T)A_L - L_B\right)L_U + k_{U_L}L_B, \quad S11$$

$$\frac{dL_B}{dt} = -k_{int_L}L_B + k_{B_L}\left((M+N+T)A_L - L_B\right)L_U - k_{U_L}L_B, \quad S12$$

$$\frac{dG_U}{dt} = \frac{p_{G,M_{\Phi I}}M_{\Phi I}}{M_{\Phi I} + \eta_{G,M\Phi}} + \frac{p_{G,M}M}{M + \eta_{G,M}} - k_{lin_G}G_U - k_{B_G}(MA_G - G_B)G_U + k_{U_G}G_B, \quad S13$$

$$\frac{dG_B}{dt} = -k_{int_G}G_B + k_{B_G}(MA_G - G_B)G_U - k_{U_G}G_B, \quad S14$$

$$\frac{dC_U}{dt} = \frac{p_{C,M}M}{M + \eta_{C,M}} - k_{lin_C}C_U - k_{B_C}(NA_C - C_B)(C_U)^{POW} + k_{U_C}C_B, \quad S15$$

$$\frac{dC_B}{dt} = -k_{int_C}C_B + k_{B_C}(NA_C - C_B)(C_U)^{POW} - k_{U_C}C_B, \quad S16$$

$$\frac{dF_U}{dt} = \frac{p_{F,I}I}{I + \eta_{F,I}} + \frac{p_{F,M_{\Phi I}}M_{\Phi I}}{M_{\Phi I} + \eta_{F,M_{\Phi I}}} + \frac{p_{F,M}M}{M + \eta_{F,M}} - k_{lin_F}F_U - k_{B_F}\left((T+I)A_F - F_B\right)F_U + k_{U_F}F_B, \quad S17$$

$$\frac{dF_B}{dt} = -k_{int_F}F_B + k_{B_F}\left((T+I)A_F - F_B\right)F_U - k_{U_F}F_B, \quad \mathrm{S18}$$

where

$$A_L = \frac{MM_L}{6.02214 \times 10^{23}}\left(K_{L,N} + K_{L,T} + K_{L,M}\right) \cdot \left(\frac{10^{-3}}{5000}\right), \quad S19$$

$$A_G = \frac{MM_G}{6.02214 \times 10^{23}} K_{G,M} \cdot \left(\frac{10^{-3}}{5000}\right), \quad S20$$

$$A_C = \hat{p}\frac{MM_C}{6.02214 \times 10^{23}} K_{C,N} \cdot \left(\frac{10^{1}}{5000}\right), \quad S21$$

$$A_F = \frac{MM_F}{6.02214 \times 10^{23}}\left(K_{F,T} + K_{F,I}\right) \cdot \left(\frac{10^{-3}}{5000}\right). \quad S22$$

S2. Model parameter values

A summary of each parameter value in **Eqs. S1-S22** is provided in **Table S1** with references. If the value was obtained through fitting, a reference to the relevant figure is provided. A summary of the variables in the model is given at the end of **Table S1**.

Table S1 Parameter values used in the Main Text. *Parameters have been grouped into: (a-e) cell related, (f-k) cytokine related parameters (l) and initial conditions. Relevant references are given estimated parameters. Parameters obtained through fitting to data in the literature have the appropriate figure noted in the Info column. Parameters estimated from homeostasis calculation are denoted by H or qualitatively estimated by E. Parameters whose value was taken from another parameters estimated has that parameter noted. Viral load is reported as virion copies and cells have been noted in* 10^9*cells. Time* t *is in days. The final sub-table (m) is a list of the variables in the model.*

a) Viral kinetic parameters

Param	Units	Description	Value	Ref	Info
p	1/day ×cop/ml /10^9cells	Lytic viral production rate	741	[1]	Fig 2
λ_S	1/day	Proliferation of epithelial cells	0.74	[2]	Fig S2
S_{max}	10^9cells	Epithelial cells carrying capacity	S_0	[3]	
$\lambda_{M\Phi}$	cop/ml/day	Production of alveolar macrophages	5943	[4]	Fig S3
$M_{\Phi max}$	10^9cells/ml	Alveolar macrophage carrying capacity	$M_{\Phi R,0}$		Fig S3
β	1/day× 1/log(cop/ml)	SARS-CoV-2 virus infection rate	0.29	[1]	Fig 2
τ_I	day	Eclipse time	0.17	[5]	
d_I	1/day	Death rate of infected cells	0.014		Fig 2
τ_T	1/day	Delay in $CD8^+$ T cell arrival	4.5	[6]	

b) Cell production, recruitment, and activation rates

Param	Units	Description	Value	Ref	Info
$p_{M_{\Phi I},G}$	1/day	Monocyte to macrophage differentiation by GM-CSF	1.7	[7]	
$p_{M_{\Phi I},L}$	1/day	Monocyte to macrophage differentiation by IL-6	1.7	[7]	
$a_{I,M\Phi}$	ml/(10^9cells)× (1/day)	Activation of macs by infected and dead cells	1.1×10^3	[8,9]	

$p_{M,I}$	1/day	Monocyte recruitment rate by infected cells	0.22	[10]	
$p_{T,F}$	1/day	$CD8^+$ T cell production rate by IFN	4	[11]	
$p_{N,L}$	1/day	Neutrophils recruitment rate by IL-6	0.21		H
$p_{T,L}$	1/day	$CD8^+$ T cells recruitment rate by IL-6	4	[11]	
$p_{T,I}$	1/day	$CD8^+$ T cell proliferation rate	1	[12]	
M^*_{prod}	1/day	Homeostasis reservoir release rate	0.13		H
ψ^{max}_M	1/day	Maximal reservoir release rate	11.55	[13]	
N^*_{prod}	1/day	Homeostasis reservoir release rate	0.21		H
ψ^{max}_N	1/day	Maximal reservoir release rate	4.13	[14]	
C^*_{BF}	—	Homeostasis neutrophil receptor bound fraction	1.6×10^{-5}	[14]	

c) Cell-related half-effect (ϵ), IC50 (IC_{50}), and Hill coefficient (h) parameters

Param	Units	Description	Value	Ref	Info
$\epsilon_{F,I}$	pg/ml	IFN inhibition of viral production	4.7×10^{-4}	[15]	
ϵ_{L,M_Φ}	pg/ml	IL-6 monocytes to macrophages	0.011	[16]	Fig S1
$\epsilon_{G,M_{\Phi I}}$	pg/ml	GM-CSF monocyte to macrophages	0.027	[17]	Fig S1
$\epsilon_{G,M}$	pg/ml	GM-CSF recruitment of monocytes	57.2	[18]	Fig S1
$\epsilon_{F,T}$	pg/ml	IFN production of $CD8^+$ T cells	0.004	[19]	Fig S1
$\epsilon_{C,N}$	unitless	G-CSF recruitment of neutrophils	1.89×10^{-4}	[14]	
$\epsilon_{L,N}$	pg/ml	IL-6 recruitment of neutrophils	57.2		$\epsilon_{G,M}$
$\epsilon_{I,M}$	10^9cells/ml	Infected cell monocyte recruitment	0.11		E
$\epsilon_{L,T}$	pg/ml	IL-6 production of $CD8^+$ T cells	3×10^{-4}	[21]	Fig S1
$\epsilon_{V,M\Phi}$	log(cop/ml)	Viral load for mac replenishing	2.96		Fig S3
$\epsilon_{T,I}$	10^9cells/ml	Antigen driven proliferation	10^{-6}	[12]	
h_M	—	GM-CSF monocyte recruitment	1.67	[18]	Fig S1
$h_{M,M\Phi}$	—	GM-CSF monocyte to macrophages	2.03	[17]	Fig S1
h_N	—	Neutrophil induced damage	3.02	[22]	Fig S1
$IC_{50,N}$	10^9cells/ml	Neutrophil induced damage	0.047	[22]	Fig S1

d) Cell/virus-induced death rates

Param	Units	Description	Value	Ref	Info
$\delta_{V,M\Phi}$	ml/(10^9cells)× 1/day	Rate of viral clearance by macrophages	768	[23]	Fig S2
$\delta_{V,N}$	ml/(10^9cells)× 1/day	Rate of viral clearance by neutrophils	2304		
δ_N	1/day	Rate of neutrophil inflicted damage	1.68	[24]	Fig S2
ρ	—	Bystander death modulation constant	0.5		E
$\delta_{I,M\Phi}$	ml/(10^9cells)× (1/day)	Rate macrophages phagocytose infected cells	121	[25]	
$\delta_{I,T}$	ml/(10^9cells)× (1/day)	Rate $CD8^+$ T cells induce apoptosis in infected cells	238	[26]	
$\delta_{M\Phi,D}$	ml/(10^9cells)× (1/day)	Rate macrophages die from phagocytosis	6.06	[27,28]	
$\delta_{D,M\Phi}$	ml/(10^9cells)× (1/day)	Rate macrophages phagocytose dead cells	8.03	[27]	Fig S2

e) Cell death and virus decay rates

Param	Units	Description	Value	Ref	Info
d_V	1/day	Viral decay rate	1.81	[29]	Fig 2
d_D	1/day	Degradation rate of apoptosed cells	8	[30]	
$d_{M_{\Phi R}}$	1/day	Alveolar macrophage death rate	0	[31]	
$d_{M_{\Phi I}}$	1/day	Inflammatory macrophage death rate	0.3	[32]	
d_M	1/day	Monocyte death rate	0.76	[33]	
d_N	1/day	Neutrophil death rate	1.28	[34]	
d_T	1/day	$CD8^+$ T cell death rate	0.4	[35]	

f) Cytokine production rates

Param	Units	Description	Value	Ref	Info
$p_{L,I}$	pg/ml/day	IL-6 production by infected cells	11.89	[36]	Fig S4
$p_{L,M_{\Phi I}}$	pg/ml/day	IL-6 production by activated macrophages	1872	[37]	Fig S4
$p_{L,M}$	pg/ml/day	IL-6 production by monocytes	72.56	[38]	Fig S1
$p_{G,M_{\Phi I}}$	pg/ml/day	GM-CSF production by inflammatory macrophages	2626	[39]	
$p_{C,M}$	ng/ml/day	G-CSF production by monocytes	26.26		$p_{G,M_{\Phi I}}$
$p_{G,M}$	pg/ml/day	GM-CSF production by monocytes cells	3070	[40]	Fig S3
$p_{F,I}$	pg/ml/day	IFN production by infected cells	2.82	[41]	Fig S3
$p_{F,M_{\Phi I}}$	pg/ml/day	IFN production by inflammatory macrophages	1.3		E
$p_{F,M}$	pg/ml/day	IFN production by monocytes	3.56	[42,43]	Fig S3

g) Cytokine production half-effect (η) and Hill coefficient (h) parameters

Param	Units	Description	Value	Ref	Info
$\eta_{L,I}$	10^9cells/ml	IL-6 production by infected cells	0.7	[36]	Fig S4
$\eta_{L,M}$	10^9cells/ml	IL-6 by monocytes	0.0045	[38]	Fig S1
$\eta_{L,M_{\Phi I}}$	10^9cells/ml	IL-6 by inflammatory macrophages	3.6×10^{-5}	[37]	Fig S4
$\eta_{G,M\Phi}$	10^9cells/ml	GM-CSF by macrophages	3.6×10^{-5}		$\eta_{L,M\Phi}$
$\eta_{G,M}$	10^9cells/ml	GM-CSF by monocytes	0.15		H
$\eta_{C,M}$	10^9cells/ml	G-CSF by monocytes	3.05		H
$\eta_{F,I}$	10^9cells/ml	IFN by infected cells	0.011	[41]	Fig S4
$\eta_{F,M_{\Phi I}}$	10^9cells/ml	IFN by inflammatory macrophages	1.3×10^{-6}		H
$\eta_{F,M}$	10^9cells/ml	IFN by monocytes	0.54	[42,43]	Fig S3

h) Cytokine linear (renal) clearance and internalization rates

Param	Units	Description	Value	Ref	Info
k_{lin_L}	1/day	Rate of IL-6 renal clearance	16.6	[44]	
k_{lin_G}	1/day	Rate of GM-CSF renal clearance	11.7	[45]	
k_{lin_C}	1/day	Rate of G-CSF renal clearance	0.16	[14]	
k_{lin_F}	1/day	Rate of IFN renal clearance	18	[46]	
k_{int_L}	1/day	Internalization rate of IL-6	61.8	[47]	Fig S2
k_{int_G}	1/day	Internalization rate of GM-CSF	73.4	[48]	
k_{int_C}	1/day	Internalization rate of G-CSF	462	[14]	
k_{int_F}	1/day	Internalization rate of IFN	17	[49]	

i) Cytokine binding/unbinding rates and stoichiometric constant

Param	Units	Description	Value	Ref	Info
k_{B_L}	ml/pg/day	IL-6 binding rate	0.0018	[50]	
k_{B_G}	ml/pg/day	GM-CSF binding rate	0.0021	[48]	
k_{B_C}	ml/ng/day	G-CSF binding rate	2.24	[14]	
k_{B_F}	ml/pg/day	IFN binding rate	0.011	[49]	
k_{U_L}	1/day	IL-6 unbinding rate	22.3	[50]	
k_{U_G}	1/day	GM-CSF unbinding rate	522	[48]	
k_{U_C}	1/day	G-CSF unbinding rate	184	[14]	
k_{U_F}	1/day	IFN unbinding rate	6.07	[49]	
POW	—	Stoichiometric constant (G-CSF)	1.4608	[51]	
		Stoichiometric constant (IL-6, GM-CSF, IFN)	1		
$\hat{p}$	—	Stoichiometry relating constant (G-CSF)	2	[51]	
		Stoichiometry relating constant (IL-6, GM-CSF, IFN)	1		

j) Number of cellular receptors and cytokine molecular weights

Param	Units	Description	Value	Ref	Info
$K_{L,N}$	sites/cell	No. IL-6 receptors on neutrophils	720	[52]	
$K_{L,T}$	sites/cell	No. IL-6 receptors on T cells	300	[53]	
$K_{L,M}$	sites/cell	No. of IL-6 receptors on monocytes	509	[54]	
$K_{G,M}$	sites/cell	No. GM-CSF receptors on monocyte	1058	[55]	
$K_{C,N}$	sites/cell	No. of G-CSF receptors on neutrophil	600	[56]	
$K_{F,T}$	sites/cell	No. of IFN receptors on T cells	1000	[57]	
$K_{F,I}$	sites/cell	No. of IFN receptors on infected cells	1300	[58]	
MM_L	g/mol	Molecular weight of IL-6	21000	[59]	
MM_G	g/mol	Molecular weight of GM-CSF	14000	[60]	
MM_C	g/mol	Molecular weight of G-CSF	19600	[14]	
MM_F	g/mol	Molecular weight of IFN-β	19000	[61]	

k) Initial conditions

Param	Units	Description	Value	Ref
V_0	$\log_{10}$(copies /ml)	Initial viral load	12	[1]
S_0	10^9 cells/ml	Initial susceptible cells	0.16	[3,62]
I_0	10^9 cells/ml	Initial infected cells	0	
R_0	10^9 cells/ml	Initial resistant cells	0	
$M_{\Phi R,0}$	10^9 cells/ml	Initial resident macrophages	2.7×10^{-5}	[3]
$M_{\Phi I,0}$	10^9 cells/ml	Initial inflammatory macrophages	2.9×10^{-7}	H
M_0	10^9 cells/ml	Initial monocytes	0.0004	[63]
M_R	10^9 cells/ml	Initial reservoir monocytes	0.0023	
N_0	10^9 cells/ml	Initial neutrophils	0.0053	[14]
N_R	10^9 cells/ml	Initial reservoir neutrophils	0.0316	[14]
T_0	10^9 cells/ml	Initial $CD8^+$ T cells	1.1×10^{-4}	[64,65]
$L_{U,0}$	pg/ml	Initial unbound IL-6	1.1	[66]
$L_{B,0}$	pg/ml	Initial bound IL-6	1.4×10^{-6}	H
$G_{U,0}$	pg/ml	Initial unbound GM-CSF	2.43	[67]
$G_{B,0}$	pg/ml	Initial bound GM-CSF	1.6×10^{-8}	H

$C_{U,0}$	ng/ml	Initial unbound G-CSF	0.025	[14]
$C_{B,0}$	ng/ml	Initial bound G-CSF	6.5×10^{-10}	[14]
$F_{U,0}$	pg/ml	Initial unbound IFN	0.015	[68]
$F_{B,0}$	pg/ml	Initial bound IFN	1.1×10^{-8}	H

m) List of variables in ***Eqs.*** **S1-S22**

Variable	Units	Description
V	cop/ml	Viral load
S	10^9 cells/ml	Susceptible cells
I	10^9 cells/ml	Infected cells
R	10^9 cells/ml	Resistant cells
$M_{\Phi R}$	10^9 cells/ml	Alveolar (resident) macrophages
$M_{\Phi I}$	10^9 cells/ml	Inflammatory macrophages
M	10^9 cells/ml	Monocytes
M_R	10^9 cells/ml	Bone marrow reservoir monocytes
N	10^9 cells/ml	Neutrophils
N_R	10^9 cells/ml	Bone marrow reservoir neutrophils
T	10^9 cells/ml	$CD8^+$ T cells
L_U	pg/ml	Unbound IL-6
L_B	pg/ml	Bound IL-6
G_U	pg/ml	Unbound GM-CSF
G_B	pg/ml	Bound GM-CSF
C_U	ng/ml	Unbound G-CSF
C_B	ng/ml	Bound G-CSF
C_{BF}	unitless	Neutrophil G-CSF receptor bound fraction
F_U	pg/ml	Unbound IFN
F_B	pg/ml	Bound IFN

S3. Parameters taken from literature

S3.1. Initial cytokine concentrations

The basal concentrations of unbound cytokines were taken from values in the literature. The plasma concentration of colony stimulating factor GM-CSF in healthy adults was measured by Lee et al.[67] to be 2.43 ± 0.42 pg/ml (i.e., $G_{U,0} = 2.43$ pg/ml). We fixed the initial unbound G-CSF cytokine concentration to $C_{U,0} = 0.025$ ng/ml [14]. The concentration of unbound IFN type 1 was set to be $F_{U,0} = 0.015$ pg/ml based on the average value of IFN-α in humans[69,70]. The median plasma IL-6 concentration was estimated to be $L_{U,0} = 1.1$ pg/ml in blood samples from healthy adults[71].

S3.2. Initial cell populations

The average total number of type I and type II alveolar epithelial cells and endothelial cells in the lung was estimated by Crapo et al.[3] to be 136×10^9 cells from eight people (6 males, 2 females) aged 19-40,. At functional residual capacity, pulmonary total tissue volume was reported by Armstrong et al.[62] to be 843 ± 110 ml. Together, this gave an initial target cell concentration of $S_0 = 0.16 \times 10^9$ cells/ml. Similarly, Crapo et al.[3] found the average number of alveolar macrophages to be $23 \pm 7 \times 10^6$ cells, thus $M_{\Phi R,0} = 2.73 \times 10^5$ cells/ml. Monocytes account for 1% to 10% of circulating white blood cells, which equates to 200 to 600 monocytes per microliter of blood[63] (with a blood volume of 5 litres[72]). Therefore, we assumed that at homeostasis $M_0 = 4 \times 10^5$ cells/ml. For the total number of neutrophils in the blood, we used the previous estimate of Craig et al.[51] $N_0 = 5.26 \times 10^6$ cells/ml that was calculated from whole blood and

marginated neutrophils. Lastly, the number of $CD8^+$ T cells in the lung tissue was, on average, 20% of the number of $CD8^+$ T cells in the blood[65]. Using flow cytometry, Uppal et al.[64] determined there were 552 cells/μl, on average, in the blood. To account for the number of naïve $CD8^+$ T cells infiltrating the lungs[73], the initial number of $CD8^+$ T cells was estimated from the proportion of T cells in the tissue, i.e. $T_0 = 1.1 \times 10^5$ cells/ml.

S3.3. Cytokine molecular weights and receptors per cell

Cytokine binding and unbinding kinetics were modelled using the molecular weight of each cytokine and the number of corresponding receptors on the binding cell. The molecular weight for IL-6 is $MM_L = 21{,}000$ g/mol[59]; for GM-CSF is $MM_G = 14{,}000$ g/mol[60]; for G-CSF is $MM_C = 19{,}600$ g/mol[51]; and for IFN-β is $MM_F = 19{,}000$ g/mol[61]. The number of high-affinity receptors for GM-CSF on the surface of blood monocytes[55] is $K_{G,M} = 1{,}058$ sites/cell. Mature human neutrophils express ~200-1,000 G-CSF receptors per cell[56], thus we fixed $K_{C,N} = 600$ sites/cell. Most cells have 1,000-2,000 type I IFN receptors (IFNAR) receptors[57]. Assuming $CD8^+$ T cells are at the lower end of this interval gives $K_{F,T} = 1{,}000$ sites/cell. The number of IFNAR sites on HEC1B human (uterus/endometrium epithelial) cells is on average $K_{F,I} = 1{,}300$ sites/cell[58]. The number of IL-6 receptors on $CD8^+$ T cells is $K_{L,T} = 300$ sites/cell based on measurements from Taga et al.[53]. We fixed the number of IL-6 receptors on neutrophils and monocytes to $K_{L,N} = 720$ sites/cell and $K_{L,M} = 509$ sites/cell respectively, based on the range in IL-6 receptors expressed on myeloma hematopoietic cells[52] and IL-6 receptors on mouse myelomonocytic leukemic M1 cells[54].

S3.4. Binding/unbinding rates of cytokines

Based on measurements by Tenhumberg et al.[50], the binding and unbinding rate of IL-6 was set to be $k_{B_L} = 0.0018$ pg/ml/day and $k_{U_L} = 22.29$/day, respectively. The unbinding kinetics for G-CSF were previously estimated by Craig et al.[51] to be $k_{U_C} = 184.87$/day. Lastly, the unbinding and binding rates for GM-CSF were taken from previous modelling work[48] and set to $k_{U_G} = 522.72$/day and $k_{B_G} = 0.0021$ per pg/ml/day respecitvely. Mager and Jusko[49] estimated the binding rate of IFN-β using a PKPD model to be $k_{B_F} = 0.0107$ per pg/ml/day. Lastly, the binding rate for GM-CSF was fixed as $k_{B_G} = 0.0021$ per pg/ml/day[48].

S3.5. Clearance and internalization rate of cytokines

Most of the clearance and internalization rates of cytokines in **Eqs. S1-S22** were obtained by assuming exponential clearance and using the half-life formula:

$$k_{lin} = \frac{\ln(2)}{t_{1/2}}, \qquad \textit{S23}$$

where $t_{1/2}$ is the cytokine half-life and k_{lin} the clearance rate. IL-6 has a short half-life of approximately 1 hour[44] giving a clearance rate of $k_{lin_L} = 16.6$/day. The half-life of GM-CSF ranges between 50-85 minutes[45]. We took the upper value giving $k_{lin_G} = 11.74$/day. The linear clearance rate of G-CSF was previously estimated by Craig et al.[51] as $k_{lin_C} = 0.16$/day. Half-lives for IFN-β range from 1-2 hours[46]. Using the lower bound, we fixed the clearance rate as $k_{lin_F} = 16.6$/day, giving a half-life of roughly 55 minutes. The internalization rates of GM-CSF and G-CSF were taken from previous pharmacokinetic modelling[48,51] and fixed to $k_{int_G} = 73.4$/day and $k_{int_C} = 462$/day. Similarly, the internalization rate of IFN was fixed as $k_{int_F} = 16.97$/day based on previous modelling of the receptor-mediated dynamics of IFN-β[46,74]. The internalization rate of IL-6, k_{lin_L}, was estimated by data fitting (Section S4.2.2).

S3.6. Neutrophil and monocyte reservoir dynamics

Craig et al.[51] previously developed a physiological model of the production dynamics of neutrophils through G-CSF regulation that accounts for the concentration of freely circulating cytokine and cytokine bound to mature neutrophils. The parameters in our model that relate to the number of neutrophils in the bone marrow reservoir, release rate, and the dynamics of G-CSF on neutrophils (**Eq. 5** & **Eq. S9**) were taken from their work, i.e. $N_R = 3.16 \times 10^7$ cells/ml, $C^*_{BF} = 1.58 \times 10^{-5}$ (unitless), $\epsilon_{C,N} = 1.8924 \times 10^{-4}$ (unitless), and $\psi_N^{max} = 4.13/\text{day}$. Similarly, the bone marrow monocyte reservoir dynamics were estimated based on previous modelling work by Cassidy et al.[13] to be $M_R = 2.27 \times 10^6$ cells/ml and $\psi_M^{max} = 11.55/\text{day}$.

S3.7. Monocyte, macrophage differentiation and activation rates

Previous mathematical modelling studies were used to estimate the monocyte and macrophage differentiation and activation rates. We assumed that the recruitment rate of monocytes would be equal to the recruitment rate of new macrophages by infected cells[10], giving $p_{M,I} = 0.22/\text{day}$. We approximated the activation rate of resident macrophages to inflammatory macrophages from the rate of dendritic cell activation[8,9], giving $a_{I,M\Phi} = 1.1 \times 10^3$ per 10^9 cells/ml/day. Lastly, the GM-CSF and IL-6 stimulated differentiation rate of monocytes to macrophages was $p_{M_{\Phi I},G} = 1.7/\text{day}$ based on the estimates that it can take 12-14 hours for monocytes to migrate from the bone marrow to the site of inflammation and subsequently differentiate into progenitor cells[7].

S3.8. $CD8^+$ T cell recruitment and expansion rate

The maximal time for $CD8^+$ T cell division is between 4-6 hours[11], giving a production rate of $p_{T,F} = 4/\text{day}$. The dynamics of $CD8^+$ T cells in response to infected cells were modelled similarly to previous work by de Pillis et al.[75] and Baral et al.[12], and we set the activation rate and half-effect parameter of infected cells from these studies, i.e. $p_{T,I} = 9 \times 10^{-3}/\text{day}$ and $\epsilon_{T,I} = 10^3$ cells/ml. Lastly, $\tau_T = 4.5$ days based on the delay in infected cell recruitment of $CD8^+$ T cells[6].

S3.9. Cell death rates

Neutrophils are known to have a short half-life in circulation[34] of $d_N = 1.28/\text{day}$. Kim et al.[35] estimated that primed $CD8^+$ T cells have a death rate of $d_T = 0.4/\text{day}$. Monocytes transiting from the bone marrow to the blood have a circulating half-life of 22 hours[33], using the half-life formula (**Eq. S23**) this gives $d_M = 0.756/\text{day}$. The time from initiation of cell apoptosis to completion can occur as quickly as 2-3 hours[30] giving a dead cell decay rate of $d_D = 8/\text{day}$. At homeostasis, mature macrophages are a quiescent population with a half-life between 4-6 weeks[31], or sometimes greater than 80 days[76]. Thus, we assumed that the death of resident alveolar macrophages is negligible ($d_{M\Phi R} = 0/\text{day}$) given the time frame of acute SARS-CoV-2 infections considered in this study (3 weeks). Inflammatory macrophages were assumed to have a death rate of $d_{M_{\Phi I}} = 0.3/\text{day}$, which was estimated through inflammatory macrophages in response to oncolytic virotherapy[32]. Macrophages also undergo apoptosis from phagocytosing too much material (exhaustion). We assumed it takes ~20 dead cells to be phagocytosed to induce macrophage death[27,28] and set $\delta_{M\Phi,D} = 6.06$ per 10^9 cells/day. The rate of $CD8^+$ T cell-induced apoptosis of infected cells was previously estimated by Lee et al.[26] giving $\delta_{I,T} = 238$ per 10^9 cells/day. The phagocytosis rate of infected cells by macrophages $\delta_{I,M\Phi} = 121.195$ per 10^9 cells/day was estimated from neutrophil phagocytosis[25].

S4. Parameters estimated by data fitting

S4.1. Pharmacodynamics of stimulatory and inhibitory effects for cells and cytokines

We used standard pharmacodynamic relationships to model the various immunological effects of cells and cytokines. Here, the half-maximal response (generally expressed as an EC_{50} or IC_{50}) of the cytokine or cell population is the concentration at which half of the maximal (stimulatory of inhibitory) effect is achieved[77]. Effect curves, E, (stimulatory or inhibitory respectively) are given by[78]

$$E = E_0 + E_{max}\frac{W^h}{W^h + EC_{50}^h}, \quad S24$$

$$E = E_0 + E_{max}\left(1 - \frac{W^h}{W^h + {IC_{50}}^h}\right), \quad S25$$

where E denotes the measured response (e.g., cell viability), W is the concentration of cytokine or cells under consideration, E_0 is the basal effect (the response when the dose of the compound is zero), E_{max} is the maximum effect (stimulatory of inhibitory) of the compound, $h > 0$ is the Hill coefficient that measures the sensitivity of the response to the dose range of the compound (i.e. the slope of the dose-response curve). **Eqs. S24-S25** are also known as Emax and Imax functions[77], see also **Eq. 1 Main Text**.

S4.1.1. *Type I IFN inhibition of viral infection and replication*

Sheahan et al.[15] measured the mean inhibition of MERS-CoV replication of IFN-β and found the EC_{50} to be 175 IU/ml. The specific activity of recombinant human IFN-β is approximately 2.8×10^8 IU/mg[15]. We converted the EC_{50} of 175 IU/ml to pg/ml to give the half-effect of IFN-β on viral production and infection capacity as $\epsilon_{F,I} = 625$ pg/ml[15]. Since this is a measurement of unbound IFN, we scaled this by the initial proportion of bound to unbound IFN ($F_{B,0}/F_{U,0}$) to get $\epsilon_{F,I} = 4.65 \times 10^{-4}$ pg/ml.

S4.1.2. *Neutrophil-induced damage of alveolar epithelial cells*

To estimate the rate of neutrophil induced damage due to the release of reactive oxygen species (ROS) (**Eqs. S2-S4**), we used cell viability measurements of rat alveolar epithelial cells (RLE) after incubation for 2 hours with hydrogen peroxide (H_2O_2) at varying concentrations[22]. Fitting **Eq. S25** to this data, we obtained $IC_{50} = 197.63\mu M$ and $h = 3.02$ (**Figure S1**A). To convert this IC_{50} from a concentration of H_2O_2 to the concentration of neutrophils (as in **Eqs. S2-S4**), we used the approximate amount of H_2O_2 produced by a single neutrophil in response to stimulation by *N*-Formylmethionyl-leucyl-phenylalanine and phorbol myristate acetate[79]. Taking the average response from these stimuli and converting to units $\mu M/cell$, neutrophils produce $0.0042\mu M$/cell of H_2O_2. As the maximum production of H_2O_2 by neutrophils is achieved relatively fast (15-30 minutes after stimulation[79]) we estimated the equivalent IC_{50} as a neutrophil concentration to be 4.71×10^4 cells (i.e. $197.62/0.0042$). As this represents a concentration of stimulated neutrophils we then increased this by the number of neutrophils at homeostasis[80] to give the half-effect concentration for neutrophil bystander damage of $IC_{50,N} = 4.71 \times 10^7$cells/ml. This estimate was in line with estimates obtained from similar experiments conducted by Weiss et al[81] and Snyers et al.[52].

S4.1.3. *Effect of GM-CSF on monocyte production and differentiation*

GM-CSF can act in a paracrine fashion to recruit circulating monocytes, enhance their functions in host defense[82,83] and influence their differentiation into monocytic or granulocytic lineages[17]. Reducing **Eqs. S8** to consider only the effect of production and differentiation gives

$$\frac{dM}{dt} = \frac{p_{M,G} {G_B}^{h_M}}{{G_B}^{h_M} + {\epsilon_{G,M}}^{h_M}} - \frac{p_{M_{\Phi I},G} {G_B}^{h_{M,M\Phi}} M}{{G_B}^{h_{M,M\Phi}} + {\epsilon_{G,M_{\Phi I}}}^{h_{M,M\Phi}}}. \quad S26$$

We modelled the effect of GM-CSF on monocyte production by estimating its potency from the dose-response of cultured blood monoculture cells with various concentrations of murine recombinant GM-CSF for 21 days[18]. Fitting **Eq. S24** gave $EC_{50} = 85.8$ IU/ml and $h = 1.67$ (**Figure S1**B). Using the specific activity of recombinant GM-CSF (i.e. 15×10^5 IU/μg [18]), this becomes $\epsilon_{G,M} = 57.2$ pg/ml. GM-CSF also promotes myeloid differentiation of cultured bone marrow cells into granulocytic and monocytic lineages towards terminal differentiation into monocytes, macrophages, and dendritic cells[17]. Sun et al.[17] investigated whether the dose of GM-CSF regulates the development of myeloid cells and measured the monocytic myeloid cell count as a function of GM-CSF concentrations. Fitting **Eq. S24** to this data, we obtained $EC_{50} = 2.66$ ng/ml and $h = 2.03$ (**Figure S1**C). Converting this to the units of GM-CSF in our model gives 2.7×10^3 pg/ml as the unbound GM-CSF half-effect concentration, which scaled by 10^{-5} (the order of initial bound GM-CSF to initial monocytes $G_{B,0}/M_0$) gives a bound GM-CSF half effect concentration of $\epsilon_{G,M\Phi} = 0.027$ pg/ml.

S4.1.1. *IL-6 production by monocytes and effect on monocyte differentiation*

Peripheral blood monocytes can be induced to secrete an array of cytokines, including IL-6, by stimuli such as lipopolysaccharide (LPS)[38]. The production of unbound IL-6 was modelled as a function of the monocyte concentration (**Eq. S11**):

$$\frac{dL_U}{dt} = \frac{p_{L,M} M}{M + \eta_{L,M}}. \quad S27$$

Alderson et al.[38] measured the concentration of IL-6 (IU/ml) produced by monocytes stimulated with 10μl of LPS over 24 hours in 1ml of culture medium (**Figure S1**D). We fit **Eq. S27** to this data by assuming the number of monocytes was fixed to $M = 2 \times 10^5$ cells and that there was no monocyte proliferation over the course of the experiment. This gave an estimate of $p_{L,M} = 7.26 \times 10^4$ pg/ml/day (converted using 4.5 pg/ml as the concentration required for half-maximal stimulation of B9 proliferation by IL-6[84]) and $\eta_{L,M} = 9 \times 10^4$ cells. Scaling this half-effect by the initial concentration of monocytes gives $\eta_{L,M} = 4.98 \times 10^7$ cells/ml. We then scaled the production rate of IL-6 by 10^3 as the maximum IL-6 concentration achieved *in vivo* during SARS-CoV-2 infection was 10^3 less than that in the two *in vitro* experiments. We confirmed this production rate using the experiments of Morris et al.[85], which measure the production of IL-6 by blood mononuclear cells by co-culturing with airway smooth muscle cells (ASM) cells and LPS stimulation.

Production of macrophages by monocytes from stimulation with IL-6 was modelled as

$$\frac{dM}{dt} = -\frac{p_{M_{\Phi I},L} L_B M}{L_B + \epsilon_{L,M_\Phi}}, \quad S28$$

$$\frac{dM_{\Phi I}}{dt} = \frac{p_{M_{\Phi I},L} L_B M}{L_B + \epsilon_{L,M_\Phi}}, \quad S29$$

where $p_{M_{\Phi I},I}$ is the production rate and $\epsilon_{L,M\Phi}$ is the half effect from the bound IL-6 (**Eqs. S7-S8**). To estimate the production of macrophages based on the concentration of IL-6, we used measurements for the production of macrophages by fibroblasts. Fibroblasts release IL-6, which then up-regulates the expression of functional M-CSF receptors on monocytes[16] and allows monocytes to consume autocrine M-CSF and thus switch differentiation to macrophages rather than DCs. Chomarat et al.[16] cultured monocytes in GM-CSF and IL-4 with graded numbers of normal skin fibroblasts. At day 5, cells were analyzed for macrophage

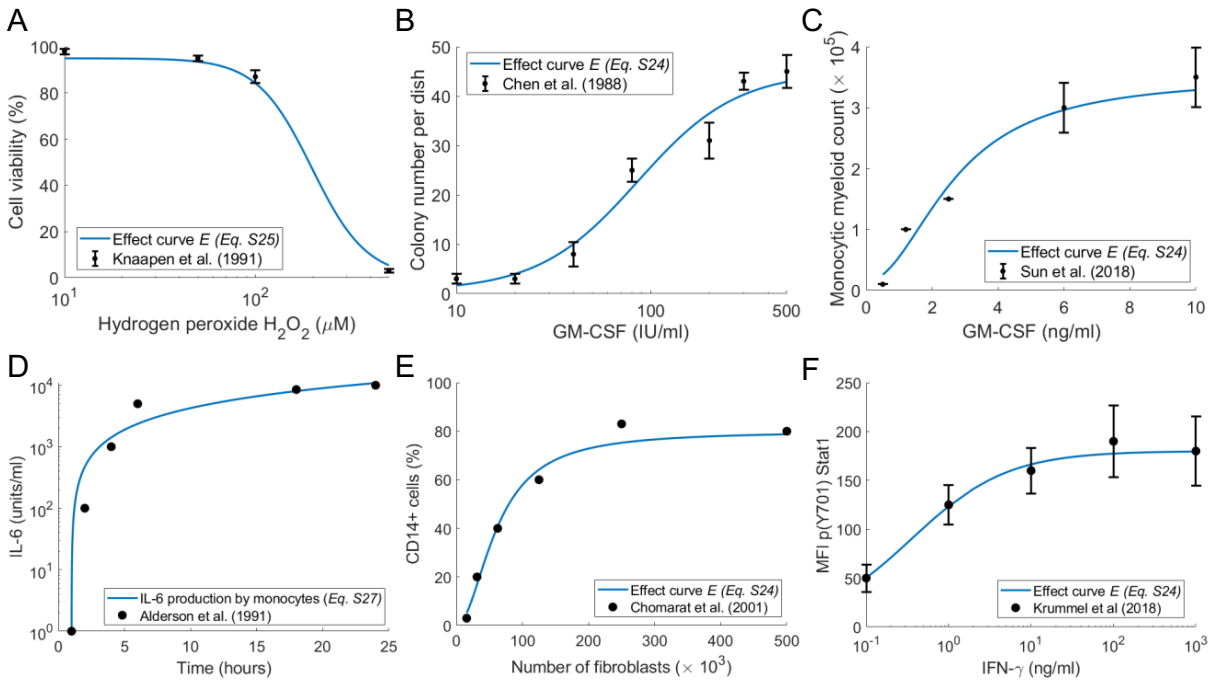

Figure S1. Effects of neutrophils on lung epithelial cells, GM-CSF on monocyte production and differentiation, the relationships between monocytes and CD4+ T cells with IL-6, and the influence of IFN on T cell expansion. *A) Using the measurements by Knaapen et al.[22], the inhibitory effect curve E (**Eq. S25**) was fit to the cell viability of RLE cells under various concentrations of H_2O_2. B) The stimulatory effect curve E (**Eq. S24**) was fit to the dose response measurements of blood monoculture cells (3×10^3 cells/dish) with various concentrations of murine recombinant GM-CSF (IU/ml)[18]. C) The stimulatory effect curve E (**Eq. S24**) was fit to measurements for the monocytic myeloid cell count as a function of GM-CSF.[17] D) **Eq. S27** fit to time course data of IL-6 production from monocytes[38]. E) IL-6 stimulation of monocyte differentiation to macrophages modelled by the inhibitory effect curve E (**Eq. S24**) fit to the percentage of CD14+ cells (macrophages) as a function of the number of fibroblasts measured by Chomarat et al.[16]. F) Stimulatory effect curve E (**Eq. S24**) for IFN-γ stimulation on CD8+ T cells fit to measurements of the signalling in CD8+T cells for varying doses of IFN-γ[19]. Data (black) is plotted as either circles (**D & E**) or mean and standard deviation error bars (**A-C&F**); solid blue line: corresponding fit.*

markers CD1a and CD14. Fitting **Eq. S24** to these results gave an $EC_{50} = 61.6$ cells and $h = 1.96$ (**Figure S1**E). Using then concentration of IL-6 produced by 250,000 fibroblasts (4.5pg/ml) and assuming that there is a linear relationship between the number of fibroblasts and the concentration of IL-6, we converted this to an unbound IL-6 concentration, i.e. $EC_{50} = 1.1 \times 10^3$ pg/ml. Scaling this by 10^{-5} (the order of initial bound to unbound IL-6 in the model) gives the bound IL-6 concentration $\epsilon_{L,M\Phi} = 0.011$ pg/ml.

S4.1.1. *Effect of IFN on CD8+ T cells*

To estimate the half-effect IFN concentration for $CD8^+$ T cell regulation, $\epsilon_{F,T}$, we used dose-response measurements for $CD8^+$ T regulation by IFN-γ. IFN-γ is known to regulate $CD8^+$ T cell differentiation through co-stimulation of the signal transducer and activator of transcription 1 (STAT1) pathway[19]. Krummel et al.[19] measured the effect on IFN-γ signaling in $CD8^+$ T cells by analysing the p(Y701) STAT1 as a function of increasing concentrations. Fitting **Eq. S24** to this data for EC_{50} and h resulting in a h value of approximately 1, so we fixed $h = 1$ to improve identifitability and fit EC_{50} which gave $EC_{50} =$ 0.4 ng/ml. Assuming the half-effect concentration for IFN-γ regulation of the STAT1 pathway can be used to estimate the half-effect concentration of IFN gives $\epsilon_{F,T} = 0.004$ pg/ml (scaled by 10^{-5} to obtain the unbound concentration; **Figure S1**F).

S4.1.1. *Effect of IL-6 on CD4$^+$ T cell expansion*

IL-6 stimulates IL-2 production and the proliferation of CD8$^+$ and CD4$^+$ T cells[21]. Holsti and Raulet[21] measured the counts per minute (CPM) of CD4$^+$ cell proliferation from IL-6 and IL-1 induction. Converting their data from sample dilution to μg/ml and fitting **Eq. S24** gave $h = 2$ and $EC_{50} = 2.26 \times 10^{-4}$ (reciprocal dilution of IL-6) (**Figure S2**A). In Holsti and Raulet, the medium contained 2.1 μg/ml of IL-6. Converting the dilution to a concentration in our units and scaling this by 10^{-5} (the order of initial bound IL-6 to unbound IL-6) gives $\epsilon_{L,T} = 4.7 \times 10^{-3}$ pg/ml.

S4.2. Estimating parameters from temporal data

S4.2.1. *Proliferation rate of epithelial cells*

We used measurements of A549 cell proliferation[2] to fit an exponential growth curve and determined the proliferation rate of epithelial cells to be $\lambda_S = 0.744$/day (**Figure S2**B).

S4.2.2. *IL-6 internalization rate*

Bound IL-6 is internalized at a rate $k_{int_L} L_B$ (**Eq. S12**), which gives the fraction of internalized IL-6

$$f(t) = 1 - e^{-k_{int_L} t}. \qquad S30$$

Fitting k_{int_L} to experiments measuring the fraction of IL-6 internalized by hepatocytes over 30 minutes[47] gave $k_{int_L} = 61.8$/day (**Figure S2**C).

S4.2.3. *Neutrophil-induced cell death rate*

To estimate the rate of epithelial cell death induced by the release of H_2O_2 by neutrophils (δ_N), we used measurements of the total alveolar macrophages apoptosis after H_2O_2 exposure from 0-12 hours[24] and fit an exponential decay rate, which gave $\delta_N = 1.68$/day (**Figure S2**D).

S4.2.4. *Rate of phagocytosis of dead cells by macrophages*

The rate macrophages phagocytose dead material is described by

$$\frac{dM_{\Phi E}}{dt} = -d_{D,M\Phi} D M_{\Phi E}, \qquad S31$$

$$\frac{dM_{\Phi F}}{dt} = d_{D,M\Phi} D M_{\Phi E}, \qquad S32$$

$$\frac{dD}{dt} = -d_{D,M\Phi} D (M_{\Phi E} - M_{\Phi F}), \qquad S33$$

where empty macrophages ($M_{\Phi E}$) phagocytose dead cells (D) at a rate $d_{D,M\Phi}$ and become loaded macrophages ($M_{\Phi F}$). Loaded macrophages also phagocytose dead cells at a rate $d_{D,M\Phi}$. Assuming the initial concentration of macrophages and dead cells is $M_{\Phi E}(0) = 36 \times 10^7$ cells/ml, $M_{\Phi F}(0) = 0$ cells/ml, and $D(0) = 5 \times 36 \times 10^7$ cells/ml (based on our full model's initial conditions and the experiment where the percentage of macrophages that had engulfed material over 25 hours was measured[27]), we fit the rate macrophages phagocytose dead material over 25 hours and obtained $d_{D,M\Phi} = 8.03$ per cell/day (**Figure S2**E).

S4.2.1. *Clearance of extracellular virus by macrophages*

To determine the clearance rate of extracellular virus by macrophages, $\delta_{V,M\Phi}$, we used measurements of foot-and-mouth disease virus (FMDV) uptake in macrophages over 2 hours *in vitro*[23] with the simple model

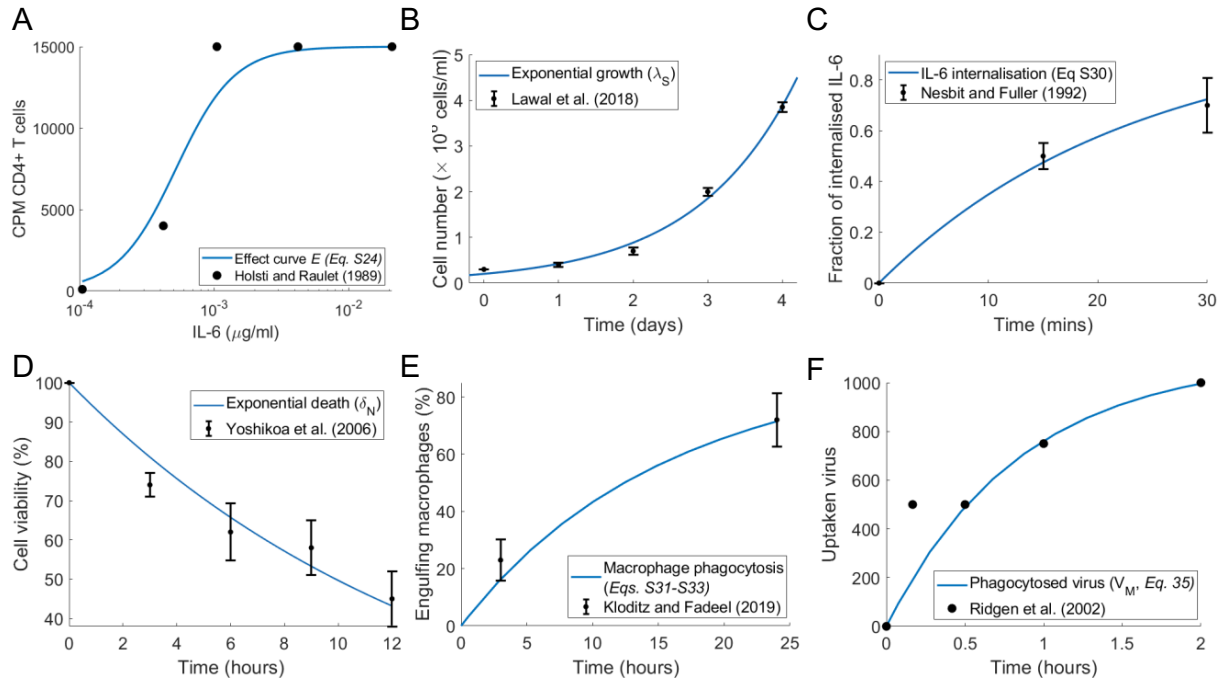

Figure S2. Dynamics of IL-6 on T cell expansion, epithelial cell growth, IL-6 internalization, neutrophil-induced damage, and macrophage phagocytosis. A) *Effect curve (**Eq. S24**) for the IL-6 effect on T cell expansion fit to measurements $CD4^+$ T cells from dilutions of IL-6 by Holsti and Raulet*[21]. ***B)*** *Exponential growth curve fit to the growth of A549 cells*[2] ***C)*** *The internalization rate of IL-6 (**Eq. S30**) fit to the fraction of internalized IL-6*[47]. ***D)*** *Exponential decay fit to cell viability after H_2O_2 administration*[24]. ***E)*** *The macrophage clearance of apoptotic material (**Eqs. S31-S33**) was fit to the percentage of macrophages that had engulfed material over 25 hours*[27]. ***F)*** *The phagocytosis rate of extracellular virus by macrophages was obtained by fitting **Eqs. S34-S35** to the uptake of virus by macrophages measured by Rigden et al.*[23]. *Data (black) is plotted as either circles (**A & F**) or mean and standard deviation error bars (**B-E**); solid blue line: corresponding fit.*

$$\frac{dV}{dt} = -\delta_{V,M\Phi} V M_{\Phi I}, \tag{S34}$$

$$\frac{dV_M}{dt} = \delta_{V,M\Phi} V M_{\Phi I}, \tag{S35}$$

where V is free virus, and V_M is the amount of phagocytosed virus. Considering $M_{\Phi I} = 36 \times 10^7$ cells/ml (i.e. our initial measurements in the lung) was constant gave an estimate of $\delta_{V,M\Phi} = 768$/day (**Figure S2**F).

S4.2.1. *Production of type I IFN by monocytes*

We modelled the production of type I IFN by monocytes (**Eq. S17**) by

$$\frac{dF_U}{dt} = \frac{p_{F,M} M}{M + \eta_{F,M}}. \tag{S36}$$

To fit the production of IFN from monocytes, we considered a simple production function for monocytes in the absence of any cytokine or inflammatory signalling

$$\frac{dM}{dt} = \frac{p_{\widehat{M}} M^h}{M^h + EC_{50,\widehat{M}}^h}\left(1 - \frac{M}{\widehat{M}_{max}}\right), \tag{S37}$$

where $p_{\widehat{M}}$ is the rate of monocyte production per day, $EC_{50,\widehat{M}}$ is the production half-effect, h is the Hill coefficient, and $\widehat{M}_{max}$ is the carrying capacity of the monocyte population. Ohta et al.[42] measured the

number of monocytes after incubation for 12 days with 0.1 nM of calcitriol. Fitting **Eq. S37** to their data, we obtained $EC_{50,\widehat{M}} = 5.4 \times 10^4$ cells, $h = 13.8$, and $\hat{p} = 9.4 \times 10^4$ cells/day (**Figure S3**A).

Krilov et al.[43] measured IFN-α production from monocytes that had been cultured for either 1, 2, 4 or 7 days before the introduction of respiratory syncytial virus (RSV). IFN-α was measured 24 hours after RSV was introduced at t_{RSV}. Combining **Eqs. S36-S37**, gives the production of IFN (F_U) from RSV stimulation of monocytes

$$\frac{d\widehat{M}}{dt} = \frac{p\widehat{M}^h}{M^h + EC_{50,\widehat{M}}^h}\left(1 - \frac{\widehat{M}}{M_{max}}\right), \quad \text{S38}$$

$$\frac{dF_U}{dt} = \frac{p_{F,M}M^h}{M^h + \eta_{F,M}^h}H(t - t_{RSV}), \quad \text{S39}$$

assuming IFN production occurs only after RVS introduction at t_{RSV}=1, 2, 4, or 7 days (modelled using the Heaviside function). Fixing $\eta_{F,M} = EC_{50,\widehat{M}} = 0.54$ pg/ml, and setting the production rate of monocytes to be equivalent to Ohta's experiments (**Figure S3**A), we fit the concentration of IFN 24 hours after *RSV* is introduced ($F_U(t_{RSV} + 24)$) and obtained $p_{F,M} = 997.1978$ IU/ml/day (**Figure S3**B). Converting the production rate using IFN's specific activity of 0.028 IU/pg gives $p_{F,M} = 3.561$ pg/ml/day

S4.2.1. *Resident macrophage production rate during declining infection*

Tissue-resident (or alveolar) macrophages return to homeostasis after viral infections have been successfully cleared[86], which we accounted for using logistic production (**Eqs. S6-S7**):

$$\frac{dV}{dt} = -d_V V, \quad \textit{S40}$$

$$\frac{dM_{\Phi R}}{dt} = \frac{\lambda_{M\Phi}M_{\Phi I}}{V + \epsilon_{V,M\Phi}}\left(1 - \frac{M_{\Phi R}}{M_{\Phi max}}\right), \quad \textit{S41}$$

$$\frac{dM_{\Phi I}}{dt} = -d_{M\Phi}M_{\Phi I} - \frac{\lambda_{M\Phi}M_{\Phi I}}{V + \epsilon_{V,M\Phi}}\left(1 - \frac{M_{\Phi R}}{M_{\Phi max}}\right). \quad \textit{S42}$$

Here $\lambda_{M\Phi}$ and $\epsilon_{V,M\Phi}$ were fit and all other parameters were fixed to their estimated values (**Table S1**).

We infected mice with 75 $TCID_{50}$ influenza A/Puerto Rico/34/8 (PR8) and measured viral loads[87] and alveolar macrophages ($F480^{hi}CD11c^{hi}CD11B^{-}$, see **Figure S3**D-E). Fitting **Eqs. S40-S42** to this data (**Figure S3**D-E) resulted in estimates of $\lambda_{M\Phi} = 0.082$ $TCID_{50}$/day, $\epsilon_{V,M\Phi} =$ 63.1 $TCID_{50}$, $M_{\Phi,max} =$ 5.02 cells, and $d_V = 1.43$/day. To convert from $TCID_{50}$ to a viral copies (RNA copy number) per volume (ml) for the units in our model, we used correlations between these (**Figure S3**C) for influenza A matrix[88]. We assumed 3.5 $TCID_{50}$ was equivalent to 2.19×10^5 virus copies[89] and took the ratio between the $TCID_{50}$ /100 µl and 10^6 copies/100 µl to be approximately 0.37 (**Figure S3**C). Thus, we set $\lambda_{M\Phi} = 5.94 \times 10^3$ copies/ml/day and $\epsilon_{V,M\Phi} =$ 905.22 copies/ml in our simulations. We validated these estimates against data from Landsman and Jung[4] (not shown).

S4.2.1. *Production of GM-CSF by monocytes*

Lee et al.[40] measured the concentration of GM-CSF produced by adherent monocytes incubated with LPS over 72 hours (**Figure S3**F). To fit to this data, we developed a simplified submodel given by

$$\frac{dM}{dt} = \frac{p_{M,G}G_B^{h_M}}{G_B^{h_M} + \epsilon_{G,M}} - d_M M, \quad \textit{S43}$$

$$\frac{dG_U}{dt} = \frac{p_{G,M}M}{M + \eta_{G,M}} - k_{lin_G}G_U - k_{B_G}(MA_G - G_B)G_U + k_{U_G}G_{B,}, \quad S44$$

$$\frac{dG_B}{dt} = -k_{int_G}G_B + k_{B_G}(MA_G - G_B)G_U - k_{U_G}G_B, \quad S45$$

where the production of monocytes (M) by bound GM-CSF (G_B) was modelled by a Hill function. Parameters were calibrated to homeostasis and we found the production rate of monocytes by GM-CSF to be $p_{M,G} = 7.29 \times 10^3$ cells/ml and the production of GM-CSF by monocytes to be $p_{G,M} = 7.7 \times 10^5$ pg/ml/day through fitting to the GM-CSF measurements of Lee et al.[40] (**Figure S3**F).

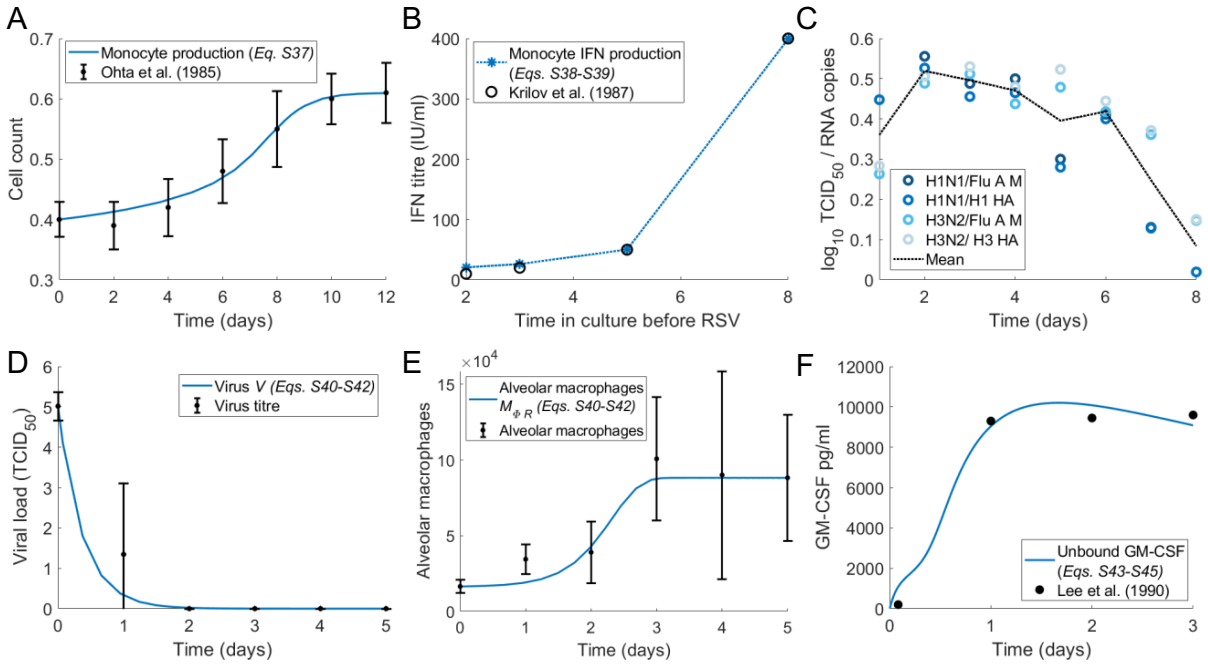

Figure S3. Monocyte expansion and type I IFN production by monocytes, alveolar macrophage replenishment after viral infection, and GM-CSF production by monocytes. A) Eq. S37 *fit to time course of proliferation of monocytes in culture[42]. **B)** Fit of **Eqs. S38-S39** to the production of IFN-α by monocytes after 24 hours with RSV as a function of the number of days of pre-culturing (1, 2, 4 or 7)[43]. **C)** Correlation between infectious virus titre and RT-PCR copy number for influenza A and B measured by Laurie et al.[88] The relative $TCID_{50}$ compared to the RNA copies is plotted for each virus strain and the mean as a black dashed line. **D-E)** Fit of **Eqs. S40-S42** to viral loads[87] and alveolar macrophages from experimental influenza infections. **F)** The production of GM-CSF from stimulated monocytes was recorded by Lee et al.[40] Using a simplified version of the full model (**Eqs. S43-S46**), we obtained the production rates for monocytes and GM-CSF. Data (black) is plotted as either circles/stars (**B&F**) or mean and standard deviation error bars (**A,D-E**); solid blue line: corresponding fit.*

S4.2.1. ***Production of IFN by infected cells***

To determine the production rate of type I IFN by infected cells, we considered all immune populations to be zero in the full model (**Eqs. S1-S22**), giving

$$\frac{dV}{dt} = pI - d_V V, \quad S46$$

$$\frac{dS}{dt} = \lambda_S\left(1 - \frac{S + I}{S_{max}}\right)S - \beta SV, \quad S47$$

$$\frac{dI}{dt} = \frac{\beta}{1 + F_B/\epsilon_{F,I}} S(t - \tau_I)V(t - \tau_I) - d_I I, \quad S48$$

$$\frac{dF_U}{dt} = \psi^*_{prod,F} + \frac{p_{F,I} I}{I + \eta_{F,I}} - k_{lin_F} F_U - k_{B_F}(IA_F - F_B)F_U + k_{U_F} F_B, \quad S49$$

$$\frac{dF_B}{dt} = -k_{int_F} F_B + k_{B_F}(IA_F - F_B)F_U - k_{U_F} F_B. \quad S50$$

Here IFN is only produced by infected cells and so there is an additional homeostatic production of IFN, $\psi^*_{prod,F}$, to account for general macrophage and monocyte production. $\psi^*_{prod,F}$ is obtained from calculating homeostasis for F_U and F_B, i.e. $dF_U/dt = dF_B/dt = 0$. Resistant cells (R) were not considered in this model as the data was only measured over 1 day. By fixing all parameters to their previously established values (**Table S1**), and fitting $p_{F,I}$ and $\eta_{F,I}$, we obtained $p_{F,I} = 2.823 \times 10^4$ pg/ml/day and $\eta_{F,I} = 0.00112$ pg/ml (**Figure S4**A). Since the concentration of IFN-α in patients infected with SARS-CoV-2 is lower than IFN-β, we reduced the production rate to $p_{F,I} = 2.823$ pg/ml/day so that model dynamics lay within the ranges of IFN-α exhibited by patients with SARS-CoV-2 infection (**Figure S6**A-B and Laing et al.[80]).

S4.2.2. *Production of IL-6 by infected cells*

To determine the rate of production of IL-6 by infected cells, Ye *et al*[36] measured the *in vitro* replication kinetics of H5N1 and H7N9 viruses in A549 cells. Cells were infected by either virus at an MOI of 2 and grown to confluence in sterile T75-tissue culture flasks (approximate cell number of 8.4×10^6)[90] and the concentration of IL-6 released from A549 cells in response to infection with both viruses was measured. We reduced the full model (**Eqs. S1-S22**) to only consider virus infection and IL-6 production by infected cells

$$\frac{dV}{dt} = pI - d_V V, \quad S51$$

$$\frac{dS}{dt} = -\beta SV, \quad S52$$

$$\frac{dI}{dt} = \beta SV - d_I I, \quad S53$$

$$\frac{dL_U}{dt} = \frac{p_{L,I} I}{I + \eta_{L,I}}. \quad S54$$

and fit to this data to obtain $p_{L,I} = 11.887$ pg/ml and $\eta_{L,I} = 0.7232 \times 10^9$ cells/ml (**Figure S4**B-C).

S4.2.3. *Production of IL-6 by alveolar macrophages*

We modelled the production of IL-6 by alveolar macrophages by

$$\frac{dL_U}{dt} = \frac{p_{L,M\Phi I} M_{\Phi I}}{M_{\Phi I} + \eta_{L,M\Phi}} \quad S55$$

to compare to observations from Shibata et al.[37] who measured the production of IL-6 by alveolar macrophages stimulated by different concentrations of LPS. Assuming no proliferation of macrophages from LPS introduction but that LPS scales the production of IL-6, we modified the above equation to be

$$\frac{dL_U}{dt} = \frac{p_{L,M_{\Phi I}} M_{\Phi \mathrm{I}}}{M_{\Phi I} + \eta_{L,M\Phi}} LPS, \qquad S56$$

and fit the Shibata et al. data and obtained $p_{L,M_{\Phi I}} = 0.078$ ng/ml/hour and $\eta_{L,M\Phi} = 4.47 \times 10^5$ cells/ml (**Figure S4**D).

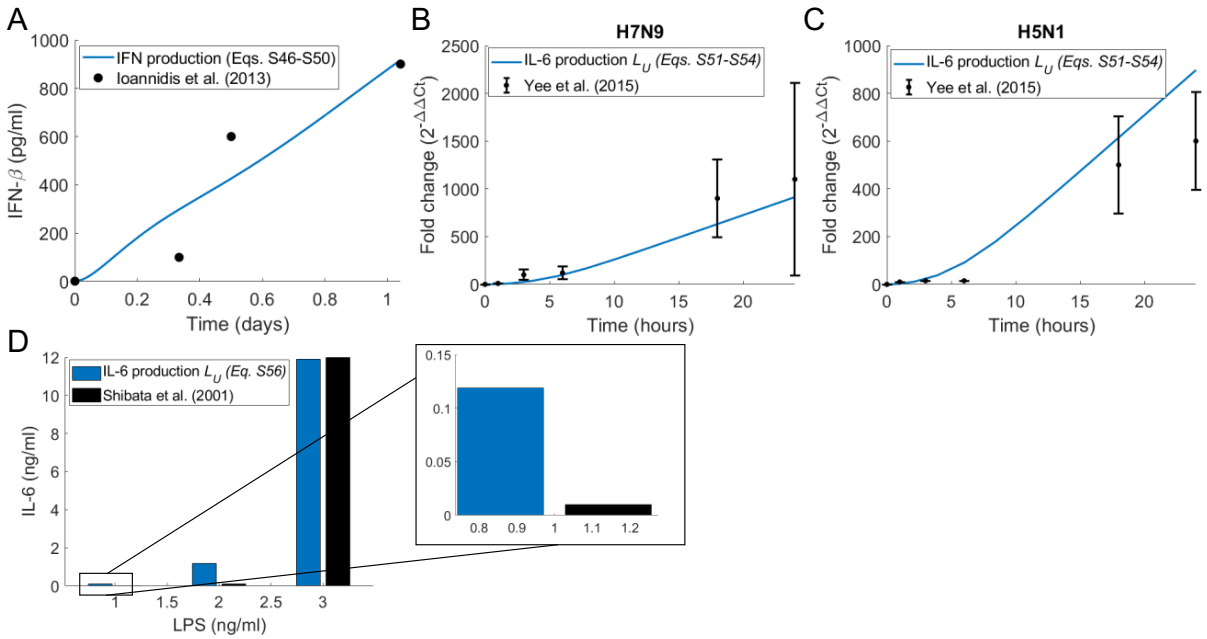

Figure S4. Production of IFN and IL-6 by infected cells and macrophages. A) *Concentration of IFN-β released by alveolar epithelial cells in response to stimulation with influenza virus recorded at 8, 16 and 24 hours[41]. **B-C)** IL-6 production by infected cells in response to **A)** H5NA and **B)** H7N9, measured by Ye et al.[36] Data (black) is plotted as mean and standard deviation error bars with the corresponding fit (**Eqs. S51-S54**) in solid blue. **D)** IL-6 production by macrophages (**Eq. S56**) in response to stimulation with LPS of varying dosage sizes. Shibata et al. [37] measured the production of IL-6 for different dosages of LPS and fitting the production rate to this data to obtain $p_{L,M\Phi}, \eta_{L,M\Phi}$.*

S5. Parameters calculated from homeostasis

Remaining parameters in the model were estimated to ensure the model maintained homeostasis in the absence of infection, i.e. we required the system to return to equilibrium state after small perturbations in initial conditions for the immune cells and cytokines. Homeostasis equations are defined below (**Eqs. S57-S70**), along with the corresponding parameter they define. These were determined by solving $d/dt = 0$. At homeostasis we assume there to be no virus and resistant cells ($V = R = 0$). Here X^* represents homeostatic values.

$$F_B(0) = F_B^* = \frac{k_{B_F} T^* A_F F_U^*}{k_{int_F} + k_{B_F} F_U^* + k_{U_F}}, \qquad S57$$

$$G_B(0) = G_B^* = \frac{k_{B_G} M^* A_G G_U^*}{k_{int_G} + k_{B_G} G_U^* + k_{U_G}}, \qquad S58$$

$$C_B(0) = C_B^* = \frac{k_{B_C} {C_U^*}^{POW_C} A_C N^*}{k_{int_C} + k_{B_C} {C_U^*}^{POW_C} + k_{U_C}}, \qquad S59$$

$$C_{BF}(0) = C_{BF}^* = \frac{C_B^*}{A_C N^*}, \qquad S60$$

$$L_B(0) = L_B^* = \frac{k_{B_L} (T^* + N^* + M^*) A_L L_U^*}{k_{int_L} + k_{B_L} L_U^* + k_{U_L}}, \qquad S61$$

$$M_{\Phi I}(0) = M^*_{\Phi I} = \frac{\left(\frac{p_{M_{\Phi \mathrm{I}},G} {G_B^*}^{h_{M,M\Phi}} M^*}{{G_B^*}^{h_{M,M\Phi}} + \epsilon_{G,M\Phi}^{\ h_{M,M\Phi}}} + \frac{p_{M_{\Phi I},L} L_B^* M^*}{L_B^* + \epsilon_{L,M\Phi}}\right)}{\left(1 - \frac{M^*_{\Phi R}}{M_{\Phi max}}\right)\frac{\lambda_{M\Phi}}{\epsilon_{V,M\Phi}} + d_{M_{\Phi \mathrm{I}}}}, \quad S62$$

$$\eta_{C,M} = \frac{p_{C,M}M^* - M^*\left(k_{lin_C} C_U^* + k_{B_C}(N^* A_C - C_B^*){C_U^*}^{POW_C} - k_{U_C} C_B^*\right)}{k_{lin_C} C_U^* + k_{B_C}(N^* A_C - C_B^*){C_U^*}^{POW_C} - k_{U_C} C_B^*}, \quad S63$$

$$p_{L,M\Phi} = \frac{M^*_{\Phi I} + \eta_{L,M\Phi}}{M^*_{\Phi I}}\left(-\frac{p_{L,M}M^*}{M^* + \eta_{L,M}} + k_{lin_L} L_U^* + k_{B_L}\left((N^* + T^* + M^*)A_L - L_B^*\right)L_U^* - k_{U_L} L_B^*\right), \quad S64$$

$$p_{G,M\Phi_I} = \frac{k_{lin_G} G_U^* + k_{B_G}(M^* A_G - G_B^*)G_U^* - k_{U_G G_B^*}}{\frac{M^*_{\Phi I}}{M^*_{\Phi I} + \eta_{G,M\Phi}} + \frac{M^*}{M^* + \eta_{G,M}}}, \quad S65$$

$$p_{M,G} = \left(\frac{{G_B^*}^{h_M} + \epsilon_{G,M}^{\ h_M}}{{G_B^*}^{h_M}}\right)\left(\frac{p_{M_{\Phi \mathrm{I}},G} {G_B^*}^{h_{M,M\Phi}} M^*}{{G_B^*}^{h_{M,M\Phi}} + \epsilon_{G,M\Phi}^{\ h_{M,M\Phi}}} + \frac{p_{M_{\Phi I},L} L_B^* M^*}{L_B^* + \epsilon_{L,M\Phi}} + d_M M^*\right), \quad S66$$

$$\eta_{F,M\Phi} = \frac{p_{F,M\Phi} M^*_{\Phi \mathrm{I}} + \left(\frac{p_{F,M}M^*}{M^* + \eta_{F,M}} - k_{lin_F} F_U^* - k_{B_F}(T^* A_F - F_B^*)F_U^* + k_{U_F} F_B^*\right) M^*_{\Phi I}}{-\frac{p_{F,M}M^*}{M^* + \eta_{F,M}} + k_{lin_F} F_U^* + k_{B_F}(T^* A_F - F_B^*)F_U^* - k_{U_F} F_B^*}, \quad S67$$

$$T^*_{prod} = d_T T^* - \frac{p_{T,L} L_B^* T^*}{L_B^* + \epsilon_{L,T}} - \frac{p_{T,F} F_B^* T^*}{F_B^* + \epsilon_{F,T}}, \quad S68$$

$$N^*_{prod} = \left(d_N N^* - \frac{p_{N_L} L_B^*}{L_B^* + \epsilon_{L,N}}\right)\frac{1}{NR}, \quad S69$$

$$M^*_{prod} = \frac{\frac{1}{MR}\left(\frac{p_{M_{\Phi I},G} {G_B^*}^{h_{M,M\Phi}} M^*}{{G_B^*}^{h_{M,M\Phi}} + \epsilon_{G,M\Phi}^{\ h_{M,M\Phi}}} + \frac{p_{M_{\Phi I},L} L_B^* M^*}{L_B^* + \epsilon_{L,M}} + d_M M^*\right) - \psi_M^{max}\frac{{G_B^*}^{h_M}}{{G_B^*}^{h_M} + \epsilon_{G,M}^{\ h_M}}}{1 - \frac{{G_B^*}^{h_M}}{{G_B^*}^{h_M} + \epsilon_{G,M}^{\ h_M}}}, \quad S70$$

The model was then simulated to confirm the parameter values determined resulted in a stable system at homeostasis (**Figure S5**).

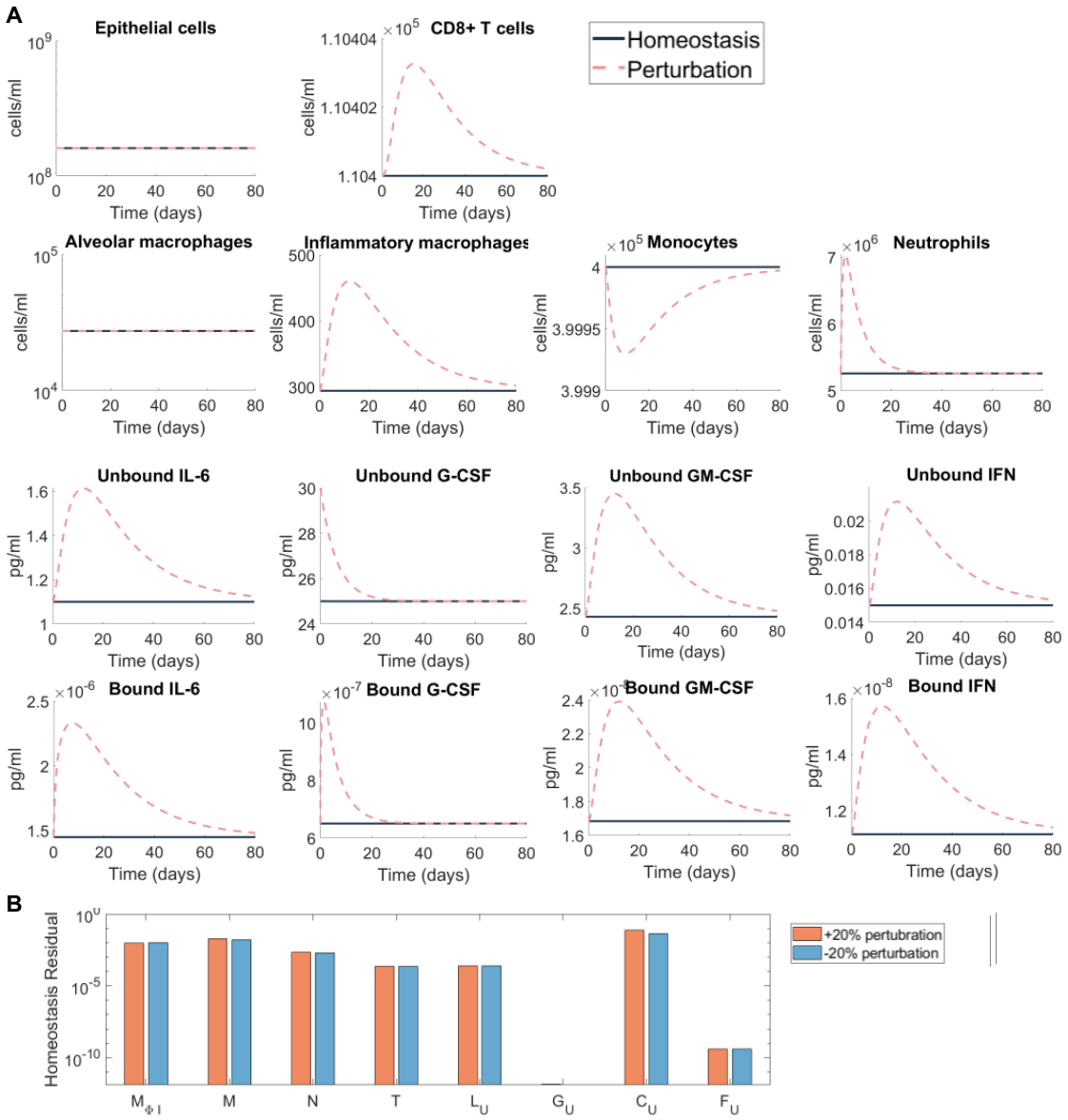

Figure S5. Homeostatic disease-free system regulation. ***A)*** *To confirm that parameters in the model represented realistic immunocompetent individuals in the disease-free scenario,* ***Eqs. S1-S22*** *were simulated where* $V_0 = 0$ *and parameters were given by the homeostasis* ***Eqs. S57-S70****. The initial concentration of G-CSF was perturbed and compared to simulations of the model at homeostasis. Simulations at homeostasis are represented by solid lines (purple) and perturbed simulations as dashed lines (pink).* ***B)*** *The maximum residual between variables and their initial conditions at day 50 was measured to confirm that the system was stable for perturbations in all immune cells and cytokines.*

S6. Model predication validation and sensitivity analysis

Having confirmed that predicted dynamics from the reduced IFN model (**Eqs. 31-37** and **Figure. 3**, **Main Text**) qualitatively matched to time-series measurements for IFN-α from Trouillet-Assant et al.[70] (**Figure S6**A), we next sought to further validate predictions of the full model by comparing IFN, IL-6, and G-CSF dynamics to previously published observations (**Figure S6**B-F). For this, measurements for IFN-$\alpha 2$ and IL-6 plasma concentrations were taken from Trouillet-Assant et al.[70] (**Figure S6**B-C), and IL-6 concentrations from patients requiring and not requiring mechanical ventilation obtained by Herold et al.[91] were also used to validate predicted IL-6 dynamics (**Figure S6**D). IL-6 and G-CSF plasma concentrations in symptomatic and asymptomatic patients were obtained by Long et al.[92] (**Figure S6**E-F). Full model simulations are given in **Figure S7**.

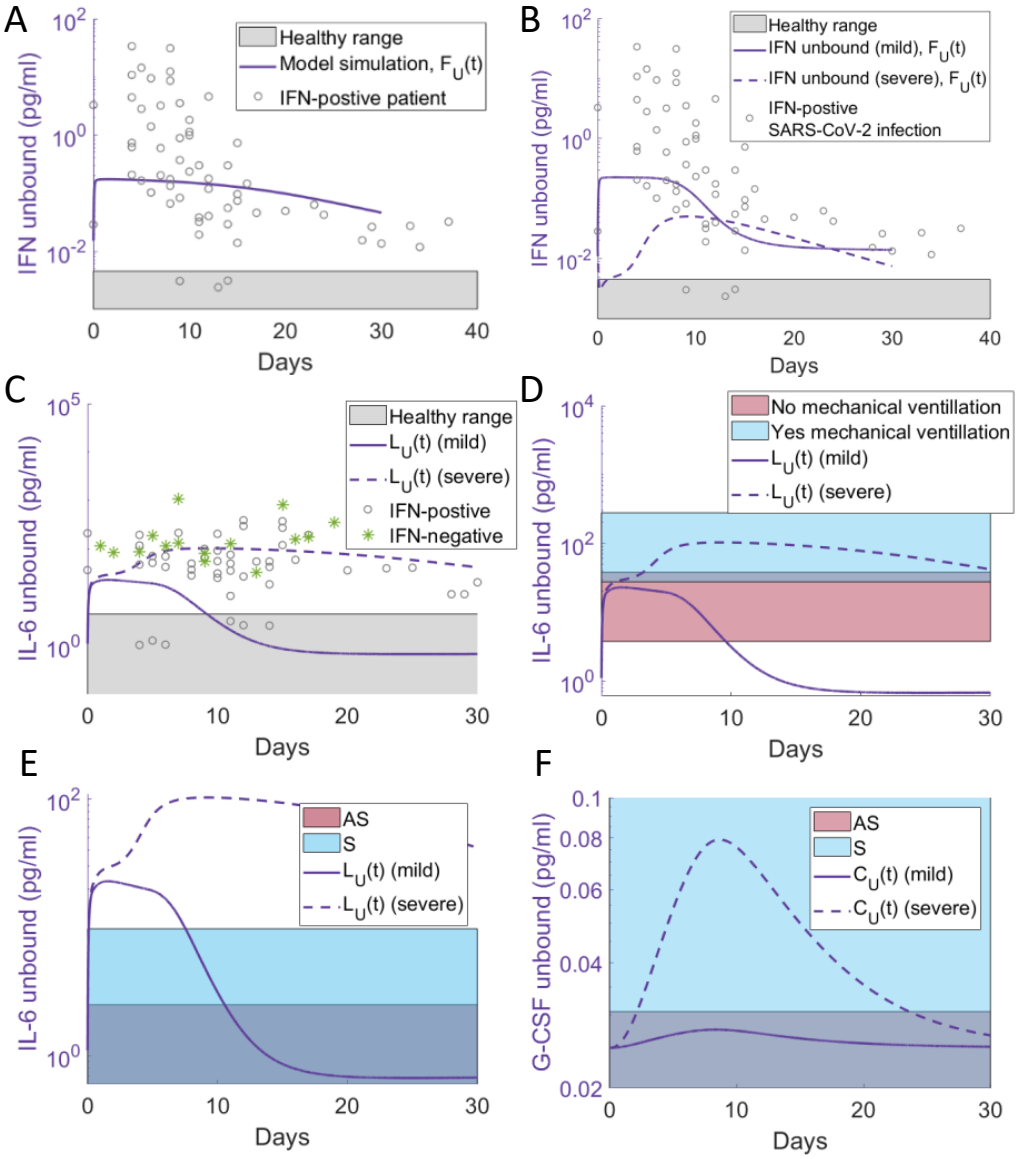

Figure S6. Model validation against human cytokine measurements during SARS-CoV-2 infection. ***A)*** *IFN dynamics of the reduced model (**Figure 3 Main Text**) overlaid with patient IFN-α2 plasma concentrations from Trouillet-Assant et al.[70] The solid line (purple) represents the unbound IFN dynamics from the reduced model (**Eqs. 27-33**). Individual patient IFN-α2 measurements are plotted as grey circles. Normal IFN-α2 concentration in healthy volunteers are indicated by a grey area.* ***B-F)*** *Mild and severe dynamics (**Eqs. S1-S22**) corresponding to simulations in **Figure 4 Main Text** and **Figure S7** overlaid with measurements from the literature with solid lines: mild disease dynamics; dashed lines: severe disease dynamics..* ***B-C)*** *Plasma IFN-α and IL-6 in COVID-19 critically ill patients (n=26) obtained by Trouillet-Assant et al.[70] overlaid with mild and severe unbound IFN ($F_U(t)$) and mild and severe unbound IL-6 ($L_U(t)$).* ***D)*** *IL-6 levels in patients requiring and not requiring mechanical ventilation obtained by Herold et al.[91] overlaid with mild and severe unbound IL-6 dynamics.* ***E-F)*** *IL-6 and G-CSF plasma concentration obtained by Long et al.[92] in symptomatic "S" and asymptomatic "AS" COVID-19 patients overlaid with corresponding mild and severe model dynamics.*

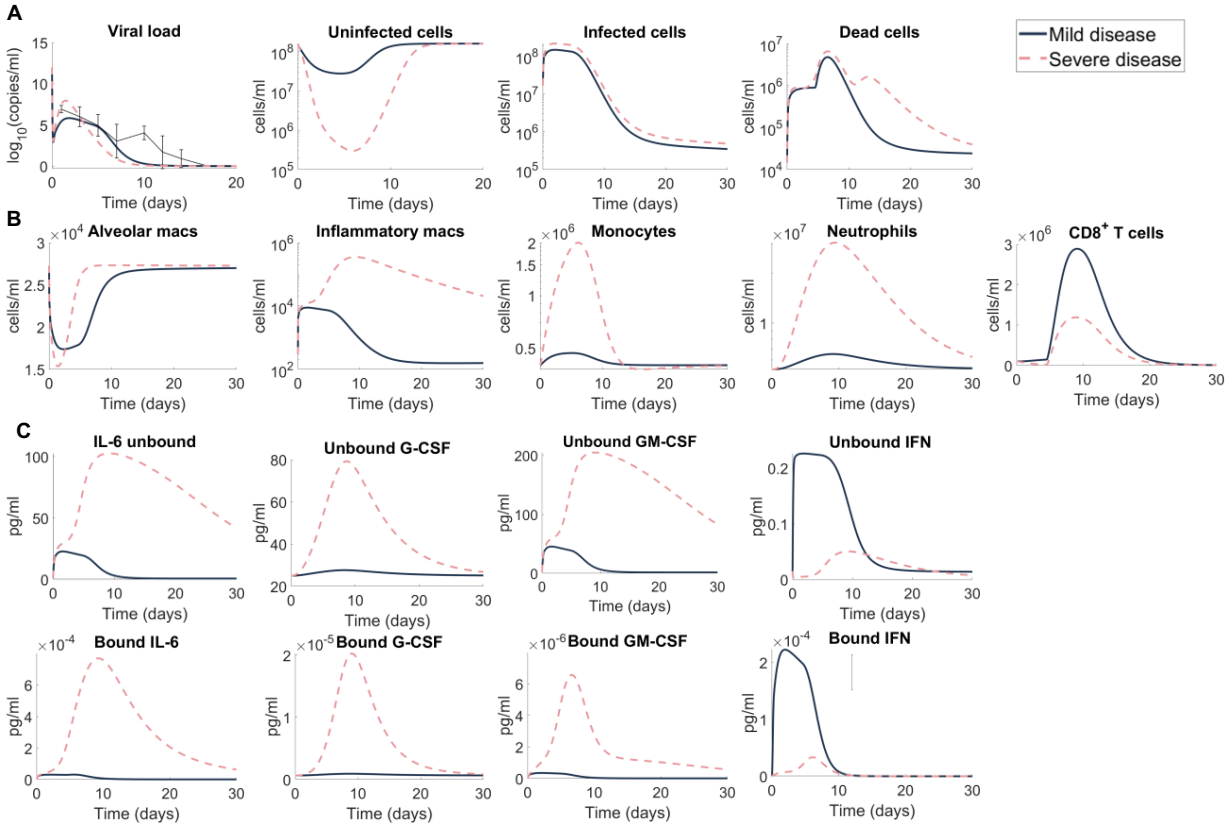

Figure S7. Predicting mild and severe COVID-19 dynamics (all model variables). *Extension of results of mild and severe disease dynamics in* ***Figure 4 Main Text****. Mild disease (solid lines) dynamics obtained by using baseline parameter estimates (****Tables S1****) while severe disease dynamics (dashed lines) were obtained by decreasing the production rate of type I IFN,* $p_{F,I}$*, and increasing the production of monocytes,* $p_{M,I}$*, and their differentiation to macrophages,* $\eta_{F,M\Phi}$*.* ***A)*** *Lung cells concentrations (susceptible cells* $S(t)$*, resistant cells* $R(t)$*, infected cells* $I(t)$*, dead cells* $D(t)$ *and virus* $V(t)$*). Solid black line with error bars indicates macaque data (see* ***Fig. 2 Main Text****).* ***B)*** *Immune cell concentrations (resident macrophages* $M_{\Phi R}(t)$*, inflammatory macrophages* $M_{\Phi I}(t)$*, monocytes* $M(t)$*, neutrophils* $N(t)$ *and T cells* $T(t)$*).* ***C)*** *Bound and unbound cytokine concentrations (IL-6 unbound* $L_U(t)$ *and bound* $L_B(t)$*, GM-CSF unbound* $G_U(t)$ *and bound* $G_B(t)$*, G-CSF unbound* $C_U(t)$ *and bound* $C_B(t)$*, type I IFN unbound* $F_U(t)$ *and bound* $F_B(t)$*).*

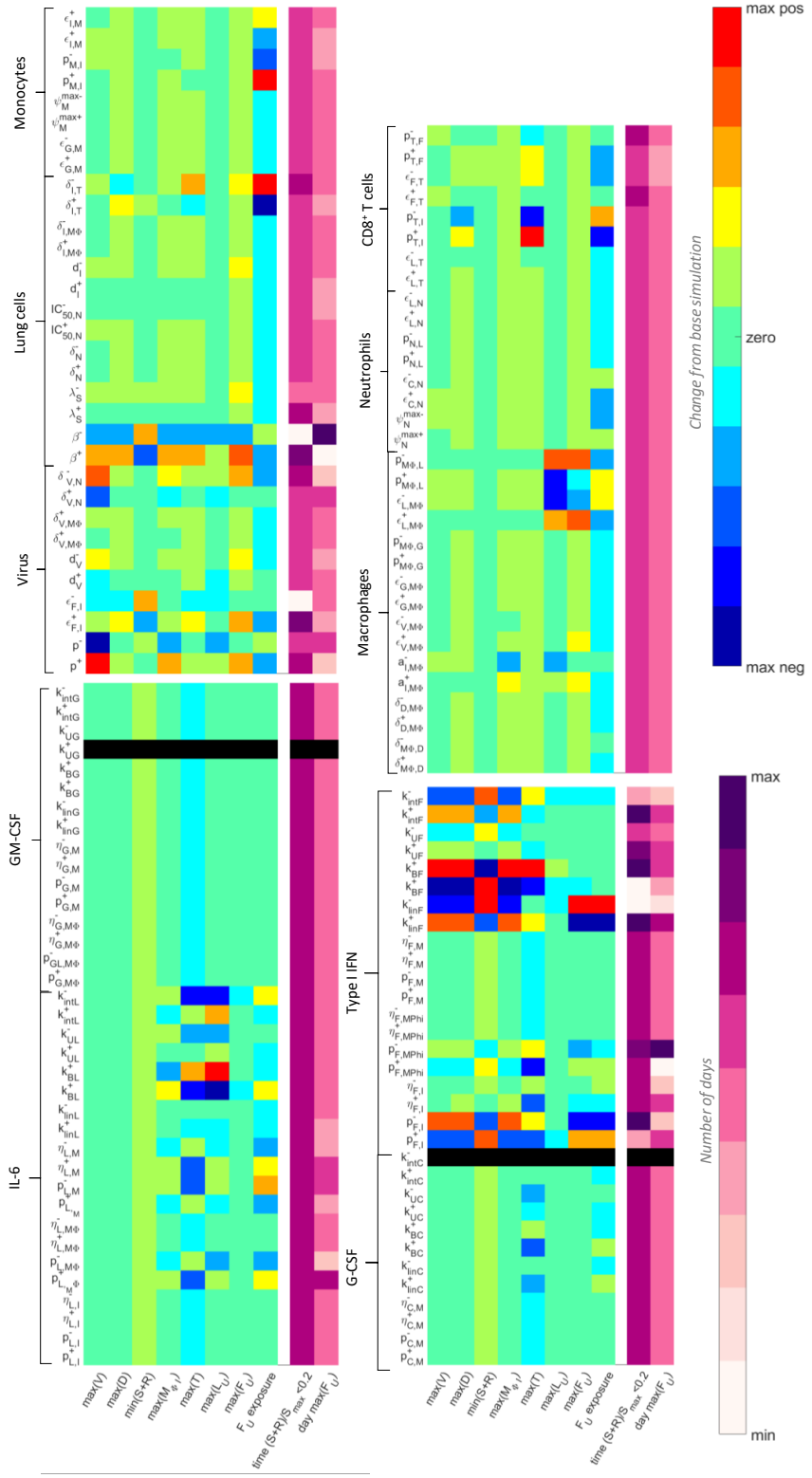

Figure S8. Full analysis of parameters driving COVID-19 severity. *A local sensitivity analysis was performed by varying each parameter ±20% from its originally estimated value and simulating the model. Predictions were then compared to baseline considering: Maximum viral load (max(V)), maximum concentration of dead cells (max(D)), minimum uninfected live cells (min(S+R)), maximum concentration of inflammatory macrophages (max($M_{\Phi I}$)), maximum number of CD8⁺ T cells (max(T)), maximum concentration of IL-6 (max(L_U)), maximum concentration of type I IFN (max(F_U)), the total exposure to type I IFN (F_U exposure), the number of days damaged tissue was >80% (time $(S + R)/S_{max}$)<0.2), and the day type I IFN reached its maximum (day max(F_U)). The heatmaps show the fold change of each metric, where blue signifies the minimum value observed and red signifies the maximum value observed, or by the number of days, where light to dark pink signifying increasing number of days from zero. The most sensitive parameters are shown in* ***Figure 5*** *in the* ***Main Text.***

S6.1. Generating of virtual patients

Initial parameter sets for each virtual patient were drawn from normal distributions with means fixed to the corresponding parameter value in **Table S1** and standard deviations derived from appropriate standard deviation or confidence interval measurements in the literature. Specifically, the standard deviation for

- the half-effect concentration of IFN on viral infectivity ($\epsilon_{F,I}$) was informed by the 95% confidence interval from fitting the Emax curve to MERS-CoV-expression nanoluciferase (nLUC) reported by Sheahan et al.[15], from the IFN-α 95% confidence interval on day 0 from Trouillet-Assant et al.[70] (**Figure S6**B-C),
- IFN production by infected cells ($p_{F,I}$ and $\eta_{F,I}$) and IFN production by macrophages ($\eta_{F,M\Phi}$) were drawn from IL-6 concentration in no mechanical ventilation patients (mild) and mechanical ventilation patients (severe) from Herold et al.[91],
- the production of IL-6 by macrophages and macrophages by IL-6 ($p_{L,M\Phi}$, and $p_{M\Phi,L}$) from Liu et al. [93] (**Figure S6**D), and
- the production of monocytes by infected cells ($p_{M,I}$), and from 95% confidence interval generated from estimating the parameter for production of IFN by monocytes[42] ($p_{F,M}$; **Figure S3**).

From normal distributions with standard deviation described above and mean as the original parameter values ($\hat{p}$), we then generated normal distributions covering 99.7% of values lying with 3 standard deviations of the mean, i.e., $[\mu - 3\sigma, \mu + 3\sigma]$[94].

After drawing an initial patient parameter set for each patient, we next used simulated annealing to determine a parameter set that resulted in patient dynamics within physiological ranges[95] for $[l_i, u_i]$ by minimising **Eq. 15**, where l_i and u_i are the upper and lower bounds extracted from measurements for viral load, type I IFN, G-CSF, and IL-6 (**Figure 7 Main Text**). The resulting parameter set from this optimization was then considered to represent a realistic patient and they were accepted into the cohort. The viral, IFN, IL-6, and G-CSF dynamics of the cohort are seen in **Figure S9**, with the physiological ranges used for optimization.

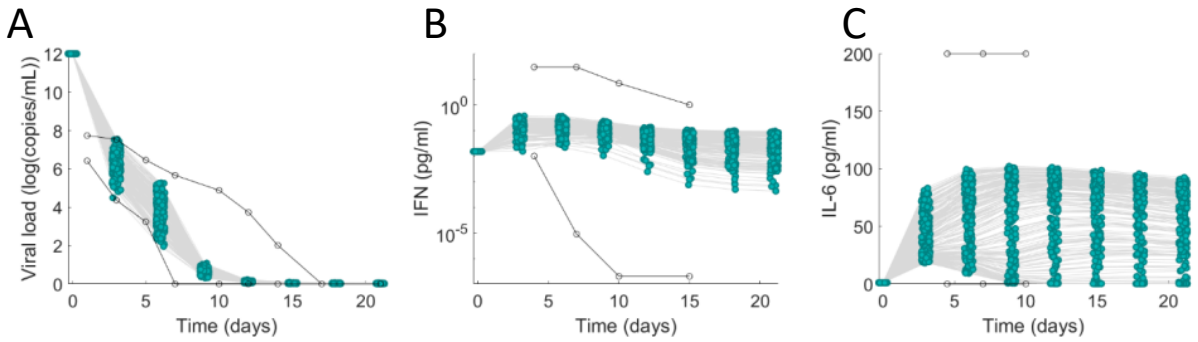

Figure S9. Cohort dynamics within physiological ranges. *Virtual patients were generated so that viral load, IFN and IL-6 concentration were within physiological ranges obtained in the literature. The physiological ranges (denoted by open circles) were obtained from* ***A)*** *Munster et al.[96],* ***B)*** *Trouillet-Assant et al. [70], and* ***C)*** *Herold et al. [91]. Patient dynamics at discrete time points are plotted as joined green dots.*

References

1. Kim, K. *et al. Modelling SARS-CoV-2 Dynamics: Implications for Therapy*. (2020). doi:10.1101/2020.03.23.20040493.
2. Lawal, O. *et al.* Volatile organic compound signature from co-culture of lung epithelial cell line with Pseudomonas aeruginosa. *Analyst* **143**, 3148–3155 (2018).
3. Crapo, J. D., Barry, B. E., Gehr, P., Bachofen, M. & Weibel, E. R. Cell number and cell characteristics of the normal human lung. *Am. Rev. Respir. Dis.* **126**, 332–337 (1982).
4. Landsman, L. & Jung, S. Lung Macrophages Serve as Obligatory Intermediate between Blood Monocytes and Alveolar Macrophages. *J. Immunol.* **179**, 3488 (2007).
5. Ng, M.-L., Tan, S.-H., See, E.-E., Ooi, E.-E. & Ling, A.-E. Proliferative growth of SARS coronavirus in Vero E6 cells. *J. Gen. Virol.* **84**, 3291–3303 (2003).
6. Janeway, C. *Immunobiology 5 : the immune system in health and disease*. (Garland Pub., 2001).
7. Kratofil, R. M., Kubes, P. & Deniset, J. F. Monocyte conversion during inflammation and injury. *Arterioscler. Thromb. Vasc. Biol.* **37**, 35–42 (2017).
8. Jenner, A. L., Frascoli, F., Yun, C.-O. & Kim, P. S. Optimising Hydrogel Release Profiles for Viro-Immunotherapy Using Oncolytic Adenovirus Expressing IL-12 and GM-CSF with Immature Dendritic Cells. *Appl. Sci.* **10**, 2872 (2020).
9. Lee, J., Adler, F. R. & Kim, P. S. A mathematical model for the macrophage response to respiratory viral infection in normal and asthmatic conditions. *Bull. Math. Biol.* **79**, 1979–1998 (2017).
10. Pawelek, K. A., Dor Jr, D., Salmeron, C. & Handel, A. Within-host models of high and low pathogenic influenza virus infections: The role of macrophages. *PLoS One* **11**, 2016 (2016).
11. Zhang, N. & Bevan, M. J. CD8+ T Cells: Foot Soldiers of the Immune System. *Immunity* **35**, 161–168 (2011).
12. Baral, S., Antia, R. & Dixit, N. M. A dynamical motif comprising the interactions between antigens and CD8 T cells may underlie the outcomes of viral infections. *Proc. Natl. Acad. Sci.* **116**, 17393 (2019).
13. Cassidy, T., Humphries, A., Craig, M. & Mackey, M. Characterizing chemotherapy-induced neutropenia and monocytopenia through mathematical modelling. *Bull. Math. Biol.* **104**, 2020.04.02.022046 (2020).
14. Craig, M., Humphries, A. R. & Mackey, M. C. A Mathematical Model of Granulopoiesis Incorporating the Negative Feedback Dynamics and Kinetics of G-CSF/Neutrophil Binding and Internalization. *Bull. Math. Biol.* **78**, 2304–2357 (2016).
15. Sheahan, T. P. *et al.* Comparative therapeutic efficacy of remdesivir and combination lopinavir, ritonavir, and interferon beta against MERS-CoV. *Nat. Commun.* **11**, 222 (2020).
16. Chomarat, P., Banchereau, J., Davoust, J. & Palucka, A. K. IL-6 switches the differentiation of monocytes from dendritic cells to macrophages. *Nat. Immunol.* **1**, 510–514 (2000).
17. Sun, L. *et al.* GM-CSF Quantity Has a Selective Effect on Granulocytic vs. Monocytic Myeloid Development and Function. *Front. Immunol.* **9**, (2018).
18. Chen, B. D., Clark, C. R. & Chou, T. H. Granulocyte/macrophage colony-stimulating factor stimulates monocyte and tissue macrophage proliferation and enhances their

responsiveness to macrophage colony-stimulating factor. *Blood* **71**, 997–1002 (1988).
19. Krummel, M. F. *et al.* Paracrine costimulation of IFN-γ signaling by integrins modulates CD8 T cell differentiation. *Proc. Natl. Acad. Sci.* **115**, 11585–11590 (2018).
20. Brandes, M., Klauschen, F., Kuchen, S. & Germain, R. N. A systems analysis identifies a feedforward inflammatory circuit leading to lethal influenza infection. *Cell* **154**, 197–212 (2013).
21. Holsti, M. A. & Raulet, D. H. IL-6 and IL-1 synergize to stimulate IL-2 production and proliferation of peripheral T cells. *J. Immunol.* **143**, 2514 (1989).
22. Knaapen, A. M. *et al.* Neutrophils cause oxidative DNA damage in alveolar epithelial cells. *Free Radic. Biol. Med.* **27**, 234–240 (1999).
23. Rigden, R. C., Carrasco, C. P., Summerfield, A. & McCullough, K. C. Macrophage phagocytosis of foot-and-mouth disease virus may create infectious carriers. *Immunology* **106**, 537–548 (2002).
24. Yoshioka, Y., Kitao, T., Kishino, T., Yamamuro, A. & Maeda, S. Nitric oxide protects macrophages from hydrogen peroxide-induced apoptosis by inducing the formation of catalase. *J. Immunol.* **176**, 4675–4681 (2006).
25. Smith, P., Wang, S.-Z., Dowling, K. & Forsyth, K. Leucocyte populations in respiratory syncytial virus-induced bronchiolitis. *J. Paediatr. Child Health* **37**, 146–151 (2001).
26. Lee, H. Y. *et al.* Simulation and Prediction of the Adaptive Immune Response to Influenza A Virus Infection □. **83**, 7151–7165 (2009).
27. Klöditz, K. & Fadeel, B. Three cell deaths and a funeral: macrophage clearance of cells undergoing distinct modes of cell death. *Cell death Discov.* **5**, 1–9 (2019).
28. Zent, C. & Elliott, M. R. Maxed out macs: physiologic cell clearance as a function of macrophage phagocytic capacity. *FEBS J.* **284**, 1021–1039 (2017).
29. Hernandez Vargas, E. A. & Velasco-Hernandez, J. X. In-host Modelling of COVID-19 Kinetics in Humans. *medRxiv* 2020.03.26.20044487 (2020) doi:10.1101/2020.03.26.20044487.
30. Elmore, S. Apoptosis: A Review of Programmed Cell Death. *Toxicol. Pathol.* **35**, 495–516 (2007).
31. Ginhoux, F. & Guilliams, M. Tissue-Resident Macrophage Ontogeny and Homeostasis. *Immunity* **44**, 439–449 (2016).
32. Eftimie, R. & Eftimie, G. Tumour-associated macrophages and oncolytic virotherapies: a mathematical investigation into a complex dynamics. *Lett. Biomath.* **5**, S6–S35 (2018).
33. Patel, A. A. *et al.* The fate and lifespan of human monocyte subsets in steady state and systemic inflammation. *J. Exp. Med.* **214**, 1913–1923 (2017).
34. Craig, M., Humphries, A. R. & Mackey, M. C. An upper bound for the half-removal time of neutrophils from circulation. *Blood* **128**, 1989–1991 (2016).
35. Kim, P. S., Lee, P. P. & Levy, D. Modeling regulation mechanisms in the immune system. *J. Theor. Biol.* **246**, 33–69 (2007).
36. Ye, S., Lowther, S. & Stambas, J. Inhibition of reactive oxygen species production ameliorates inflammation induced by influenza A viruses via upregulation of SOCS1 and SOCS3. *J. Virol.* **89**, 2672–2683 (2015).
37. Shibata, Y. *et al.* GM-CSF Regulates Alveolar Macrophage Differentiation and Innate Immunity in the Lung through PU.1. *Immunity* **15**, 557–567 (2001).
38. Alderson, M. R., Tough, T. W., Ziegler, S. F. & Grabstein, K. H. Interleukin 7 induces cytokine secretion and tumoricidal activity by human peripheral blood monocytes. *J. Exp.*

Med. **173**, 923–930 (1991).
39. Hallsworth, M. P., Soh, C. P., Lane, S. J., Arm, J. P. & Lee, T. H. Selective enhancement of GM-CSF, TNF-alpha, IL-1 beta and IL-8 production by monocytes and macrophages of asthmatic subjects. *Eur. Respir. J.* **7**, 1096 (1994).
40. Lee, M.-T., Kaushansky, K., Ralph, P. & Ladner, M. B. Differential Expression of M-CSF, G-CSF, and GM-CSF by Human Monocytes. *J. Leukoc. Biol.* **47**, 275–282 (1990).
41. Ioannidis, I., Ye, F., McNally, B., Willette, M. & Flaño, E. Toll-Like Receptor Expression and Induction of Type I and Type III Interferons in Primary Airway Epithelial Cells. *J. Virol.* **87**, 3261 (2013).
42. Ohta, M., Okabe, T., Ozawa, K., Urabe, A. & Takaku, F. 1α,25-Dihydroxy vitamin D_3 (calcitriol) stimulates proliferation of human circulating monocytes in vitro. *FEBS Lett.* **185**, 9–13 (1985).
43. Krilov, L. R., Hendry, R. M., Godfrey, E. & McIntosh, K. Respiratory Virus Infection of Peripheral Blood Monocytes: Correlation with Ageing of Cells and Interferon Production in vitro. *J. Gen. Virol.* **68**, 1749–1753 (1987).
44. Mehra, R. *et al.* Soluble interleukin 6 receptor: a novel marker of moderate to severe sleep-related breathing disorder. *Arch. Intern. Med.* **166**, 1725–1731 (2006).
45. Stagg, J., Wu, J. H., Bouganim, N. & Galipeau, J. Granulocyte-Macrophage Colony-Stimulating Factor and Interleukin-2 Fusion cDNA for Cancer Gene Immunotherapy. *Cancer Res.* **64**, 8795 (2004).
46. Arnaud, P. Different interferons: Pharmacology, pharmacokinetics, proposed mechanisms, safety and side effects. *Rev. Med. Interne* **23**, 449S-458S (2002).
47. Nesbitt, J. E. & Fuller, G. M. Dynamics of interleukin-6 internalization and degradation in rat hepatocytes. *J. Biol. Chem.* **267**, 5739–5742 (1992).
48. Nicola, N. A., Peterson, L., Hilton, D. J. & Metcalf, D. Cellular processing of murine colony-stimulating factor (Multi-CSF, GM-CSF, G-CSF) receptors by normal hemopoietic cells and cell lines. *Growth Factors* **1**, 41–49 (1988).
49. Mager, D. E. & Jusko, W. J. Receptor-Mediated Pharmacokinetic/Pharmacodynamic Model of Interferon-β 1a in Humans. *Pharm. Res.* **19**, 1537–1543 (2002).
50. Tenhumberg, S. *et al.* Structure-guided Optimization of the Interleukin-6 Trans-signaling Antagonist sgp130. *J. Biol. Chem.* **283**, 27200–27207 (2008).
51. Craig, M., Humphries, A. R. & Mackey, M. C. A Mathematical Model of Granulopoiesis Incorporating the Negative Feedback Dynamics and Kinetics of G-CSF/Neutrophil Binding and Internalization. *Bull. Math. Biol.* **78**, 2304–2357 (2016).
52. Snyers, L. U. C., Fontaine, Vér. & Content, J. Modulation of Interleukin-6 Receptors in Human Cellsa. *Ann. N. Y. Acad. Sci.* **557**, 388–395 (1989).
53. Taga, T., Kawanishi, Y., Hardy, R. R., Hirano, T. & Kishimoto, T. Receptors for B cell stimulatory factor 2. Quantitation, specificity, distribution, and regulation of their expression. *J. Exp. Med.* **166**, 967–981 (1987).
54. Yamaguchi, M. *et al.* Down-regulation of interleukin 6 receptors of mouse myelomonocytic leukemic cells by leukemia inhibitory factor. *J. Biol. Chem.* **267**, (1992).
55. Chiba, S. *et al.* Characterization and molecular features of the cell surface receptor for human granulocyte-macrophage colony-stimulating factor. *Leukemia* **4**, 29 (1990).
56. Barreda, D. R., Hanington, P. C., Belosevic, M. & Belosevic, M. Regulation of myeloid development and function by colony stimulating factors. *Dev. Comp. Immunol.* **28**, 509–554 (2004).

57. Branca, A. A. Interferon receptors. *Vitr. Cell. Dev. Biol.* **24**, 155–165 (1988).
58. Constantinescu, S. N. *et al.* Role of interferon α/β receptor chain 1 in the structure and transmembrane signaling of the interferon α/β receptor complex. *Proc. Natl. Acad. Sci. U. S. A.* **91**, 9602–9606 (1994).
59. Recombinant human interleukin-6 (with HSA). vol. 2020.
60. Razelle, K. Granulocyte-macrophage colony-stimulating factor. *Holland-Frei Cancer Medicine* vol. 6 (2003).
61. IFN-beta recombinant protein :: Interferon-beta 1a Recombinant Protein. vol. 2020.
62. Armstrong, J. D., Gluck, E. H., Crapo, R. O., Jones, H. A. & Hughes, J. M. B. Lung tissue volume estimated by simultaneous radiographic and helium dilution methods. *Thorax* **37**, 676–679 (1982).
63. Chaffey, N. Alberts, B., Johnson, A., Lewis, J., Raff, M., Roberts, K. and Walter, P. Molecular biology of the cell. 4th edn. *Ann. Bot.* **91**, 401 (2003).
64. Uppal, S., Verma, S. & Dhot, P. Normal values of CD4 and CD8 lymphocyte subsets in healthy indian adults and the effects of sex, age, ethnicity, and smoking. *Cytom. Part B Clin. Cytom. J. Int. Soc. Anal. Cytol.* **52**, 32–36 (2003).
65. Gordon, C. L. *et al.* Tissue reservoirs of antiviral T cell immunity in persistent human CMV infection. *J. Exp. Med.* **214**, 651–667 (2017).
66. Maes, M. *et al.* Elevated serum interleukin-6 (IL-6) and IL-6 receptor concentrations in posttraumatic stress disorder following accidental man-made traumatic events. *Biol. Psychiatry* **45**, (1999).
67. Lee, J., Kim, Y., Lim, J., Kim, M. & Han, K. G-CSF and GM-CSF concentrations and receptor expression in peripheral blood leukemic cells from patients with chronic myelogenous leukemia. *Ann. Clin. Lab. Sci.* **38**, 331–337 (2008).
68. Suzuki, K. *et al.* Circulating cytokines and hormones with immunosuppressive but neutrophil-priming potentials rise after endurance exercise in humans. *Eur. J. Appl. Physiol.* **81**, 281–287 (2000).
69. Rodero, M. P. *et al.* Detection of interferon alpha protein reveals differential levels and cellular sources in disease. *J. Exp. Med.* **214**, 1547–1555 (2017).
70. Trouillet-Assant, S. *et al.* Type I IFN immunoprofiling in COVID-19 patients. *J. Allergy Clin. Immunol.* 4–8 (2020) doi:10.1016/j.jaci.2020.04.029.
71. Kasperska-Zajac, A., Sztylc, J., Machura, E. & Jop, G. Plasma IL-6 concentration correlates with clinical disease activity and serum C-reactive protein concentration in chronic urticaria patients. *Clin. Exp. Allergy* **41**, 1386–1391 (2011).
72. Sharma, R. & Sharma, S. Physiology, Blood Volume. in *StatPearls [Internet]* (StatPearls Publishing, 2018).
73. Cose, S., Brammer, C., Khanna, K. M., Masopust, D. & Lefrançois, L. Evidence that a significant number of naive T cells enter non-lymphoid organs as part of a normal migratory pathway. *Eur. J. Immunol.* **36**, 1423–1433 (2006).
74. Mager, D. & Jusko, W. Development of translational pharmacokinetic--pharmacodynamic models. *Clin. Pharmacol. Ther.* **83**, 909–912 (2008).
75. de Pillis, L. *et al.* Mathematical model creation for cancer chemo-immunotherapy. *Comput. Math. Methods Med.* **10**, 165–184 (2009).
76. Tura, S., Cavo, M. & Zinzani, P. L. *Hematology. Pathophysiology, Diagnosis and Treatment*. (2018).
77. Jones, G. Fitting and handling dose response data. *J. Comput. Aided. Mol. Des.* **29**, 1–11

(2015).
78. Macdougall, J. Analysis of dose--response studies—E max model. in *Dose finding in drug development* 127–145 (2006).
79. Smith, R. J. & Bowman, B. J. Generation of hydrogen peroxide by human neutrophils: effects of soluble stimuli and requirements for divalent cations. *Clin. Immunol. Immunopathol.* **24**, 194–203 (1982).
80. Laing, A. G. *et al.* A dynamic COVID-19 immune signature includes associations with poor prognosis. *Nat. Med.* (2020) doi:10.1038/s41591-020-1038-6.
81. Weiss, S. J., Young, J., LoBuglio, A. F., Slivka, A. & Nimeh, N. Role of hydrogen peroxide in neutrophil-mediated destruction of cultured endothelial cells. *J. Clin. Investig.* **68**, 714–721 (1981).
82. Shi, Y. *et al.* Granulocyte-macrophage colony-stimulating factor (GM-CSF) and T-cell responses: what we do and don't know. *Cell Res.* **16**, 126–133 (2006).
83. Rösler, B. & Herold, S. Lung epithelial GM-CSF improves host defense function and epithelial repair in influenza virus pneumonia—a new therapeutic strategy? *Mol. Cell. Pediatr.* **3**, 29 (2016).
84. Pignatti, P. *et al.* High circulating levels of biologically inactive IL-6/SIL-6 receptor complexes in systemic juvenile idiopathic arthritis: evidence for serum factors interfering with the binding to gp130. *Clin. Exp. Immunol.* **131**, 355–363 (2003).
85. Morris, G. E. *et al.* Agonists of toll-like receptors 2 and 4 activate airway smooth muscle via mononuclear leukocytes. *Am. J. Respir. Crit. Care Med.* **171**, 814–822 (2005).
86. Denney, L. & Ho, L.-P. The role of respiratory epithelium in host defence against influenza virus infection. *Biomed. J.* **41**, 218–233 (2018).
87. Smith, A. P., Moquin, D. J., Bernhauerova, V. & Smith, A. M. Influenza virus infection model with density dependence supports biphasic viral decay. *Front. Microbiol.* **9**, 1554 (2018).
88. Laurie, K. L. *et al.* Interval between infections and viral hierarchy are determinants of viral interference following influenza virus infection in a ferret model. *J. Infect. Dis.* **212**, 1701–1710 (2015).
89. Cao, P. *et al.* Innate immunity and the inter-exposure interval determine the dynamics of secondary influenza virus infection and explain observed viral hierarchies. *PLoS Comput. Biol.* **11**, (2015).
90. Lam, W., Yeung, A. C., Chu, I. M. & Chan, P. K. Profiles of cytokine and chemokine gene expression in human pulmonary epithelial cells induced by human and avian influenza viruses. *Virol. J.* **7**, 344 (2010).
91. Herold, T. *et al.* Elevated levels of interleukin-6 and CRP predict the need for mechanical ventilation in COVID-19. *J. Allergy Clin. Immunol.* (2020).
92. Long, Q.-X. *et al.* Clinical and immunological assessment of asymptomatic SARS-CoV-2 infections. *Nat. Med.* 1–5 (2020).
93. Liu, J. *et al.* Longitudinal characteristics of lymphocyte responses and cytokine profiles in the peripheral blood of SARS-CoV-2 infected patients. *EBioMedicine* 102763 (2020).
94. Cassidy, T. & Craig, M. Determinants of combination GM-CSF immunotherapy and oncolytic virotherapy success identified through in silico treatment personalization. *PLoS Comput. Biol.* **15**, (2019).
95. Allen, R. J., Rieger, T. R. & Musante, C. J. Efficient Generation and Selection of Virtual Populations in Quantitative Systems Pharmacology Models. *CPT Pharmacometrics Syst.*

Pharmacol. **5**, 140–146 (2016).
96. Munster, V. J. *et al.* Respiratory disease in rhesus macaques inoculated with SARS-CoV-2. *Nature* (2020) doi:10.1038/s41586-020-2324-7.